journal

J. Am. Ceram. Soc., 80 [9] 2367–81 (1997)

Role of Microstructure in Hertzian Contact Damage in Silicon Nitride: I, Mechanical Characterization

Seung Kun Lee,*,† Sataporn Wuttiphan, and Brian R. Lawn*

Materials Science and Engineering Laboratory, National Institute of Standards and Technology, Gaithersburg, Maryland 20899

In this Part I of a two-part study of Hertzian indentation in silicon nitride we characterize irreversible contact damage as a function of microstructure. Three controlled silicon nitride microstructures are examined, representing a progression toward greater long-crack toughness: fine (*F*), bimodal with predominantly equiaxed α grains; medium (*M*), bimodal with mostly β grains of intermediate size; and coarse (*C*), with almost exclusively elongated β grains. An effect of increasing the microstructural heterogeneity in this sequence is to suppress ring cracking around the indenter, ultimately to a degree beyond that expected from increased toughness alone. Along with the crack suppression is a parallel tendency to enhanced damage accumulation beneath the indenter, such that the contact in the coarsest microstructure is predominantly quasi-plastic. The characterization of damage includes the following: determination of indentation stress–strain curves, to measure the level of quasi-plasticity; measurement of threshold loads for the initiation of ring cracking and subsurface yield, to quantify the competing damage processes; and measurement of characteristic dimensions of the ensuing cracks and deformation zones in their well-developed stages. These quantitative results are considered in terms of formal contact mechanics, along with finite element modeling to generate the essentially elastic–plastic fields in the different silicon nitride structures. This contact mechanics description serves also as the basis for subsequent analysis of strength degradation in Part II. Implications concerning microstructural design of silicon nitride ceramics for specific applications, notably bearings, are considered.

I. Introduction

SILICON NITRIDE is acknowledged as the ceramic of first choice for modern bearing applications where resistances to wear, fatigue, and corrosion are limiting factors in lifetime performance.[1,2] At the same time, it is well recognized that the toughness of silicon nitride ceramics can be profoundly increased by suitably tailoring the microstructures, e.g., by growing large elongated grains[3–6] and by manipulating the grain boundary phase,[7,8] in order to enhance bridging.[6,9,10] However, this toughness increase is generally limited to the long-crack region. Properties determined at the microstructural level, among them strength, may undergo simultaneous degradation[11–14]—in extreme cases such degradation may be sufficiently pronounced as to render the ceramic ''machinable.''[15] At issue here is whether increased heterogeneity in the silicon nitride microstructure results in more pronounced damage in concentrated loadings. In the specific context of optimal bearing design, there is a clear need to understand the role of internal microstructural variables on damage properties.

Hertzian testing with spherical indenters is an especially powerful tool for providing insight into these implied microstructural tradeoffs.[16] The Hertzian test has been used in the damage characterization of several tough ceramics,[17–21] including initial studies on silicon nitride.[22–25] By virtue of its highly confined, compression-dominated stress field, this test uniquely allows for the identification of intrinsic damage modes that are not ordinarily evident in conventional fracture specimens, but which are nevertheless crucial to bearing performance. Essentially, the consequence of increasing microstructural heterogeneity, with accompanying microscale weakness, is a change from classic tension-driven ring or cone cracking outside the contact to shear-driven distributed damage beneath the contact, constituting an effective brittle-to-ductile transition.[16,26] This transition accounts for the higher susceptibility to fatigue and wear mentioned above. The Hertzian test is also open to quantification, via measurement of indentation stress–strain curves[18,19,27,28] and finite element modeling (FEM) of fracture and deformation zones.[29]

In this study we examine Hertzian contact damage in controlled silicon nitride microstructures. We consider three grades of silicon nitride with progressively increasing grain size, designated fine (*F*), medium (*M*), and coarse (*C*), of which the second most closely represents conventional bearing-grade silicon nitride. This microstructural progression also represents increasing grain elongation and β/α phase ratio. The study is presented in two parts. In Part I, Hertzian tests are made to characterize the basic contact damage modes in each material grade, in particular the competition between brittle fracture and quasi-plastic deformation. The observed damage patterns are subjected to quantitative mechanical analysis, using FEM to map out macroscopic ''yield'' zones and fracture mechanics to determine conditions for ring crack initiation and propagation. The principal contact variables are sphere radius, *r*, and load, *P*.

In Part II, the degrading effect of contact damage on strength will be evaluated.

II. Processing and Preparatory Characterization of Silicon Nitride Materials

Silicon nitride materials with three microstructures were processed from a common starting powder composition by controlled heat treatment, and then routinely characterized for subsequent Hertzian testing. Parameters determined from this characterization are included in Table I.

(1) Processing

The starting silicon nitride powder composition consisted of α-Si_3N_4 (UBE-SN-E10, Ube Industries, Tokyo, Japan) with the

G. M. Pharr—contributing editor

Manuscript No. 191531. Received September 4, 1996; approved February 24, 1997.

Based in part on the Ph.D. dissertation submitted by S. Wuttiphan to the Department of Materials and Nuclear Engineering, University of Maryland, College Park, MD.

Supported by the U.S. Air Force Office of Scientific Research.

*Member, American Ceramic Society.

†Guest Scientist, from the Department of Materials Science and Engineering, Lehigh University, Bethlehem, Pennsylvania 18015.

Table I. Silicon Nitride Data

Material	*F*-Si_3N_4	*M*-Si_3N_4	*C*-Si_3N_4	WC
Hot-press condition	1570°C, 1 h	1650°C, 1 h	1800°C, 3 h	
Grain morphology	Equiaxed, elongated†	Equiaxed, elongated†	Elongated†	
Grain size (μm)†	0.4 (equiaxed) 1.5/0.4 (elongated)	0.5 (equiaxed) 4.0/0.5 (elongated)	9.0/1.5	
β-phase (vol%)	17	78	100	
Hardness, *H* (GPa)	21.0 ± 0.7	17.9 ± 0.4	15.8 ± 1.1	19.0
Toughness, *T* (MPa · $m^{1/2}$)	3.9 ± 0.3	5.3 ± 0.4	4.5–7.0‡	
Strength, σ_F (MPa)	885 ± 85	1084 ± 62	792 ± 32	
Flaw size, c_f (μm)	5 ± 2	6 ± 2	9 ± 4	
Young's modulus, *E* (GPa)	335	326	315	614
Poisson's ratio, ν	0.27	0.28	0.29	0.22
Yield stress, *Y* (GPa)	11.7	9.5	7.3	6.0
Strain-hardening coefficient	1.0	0.7	0.5	0.1

†Length/diameter of rodlike grains. ‡*R*-curve, crack extension range 40–700 μm.

following additives: 5 wt% Y_2O_3 (Fine Grade, H. C. Starck GmbH, Goslar, Germany), 2 wt% Al_2O_3 (AKP 50, Sumitomo Chemical Co. Ltd., Tokyo, Japan), and 1 wt% MgO (High Purity, Baikowski Co., Charlotte, NC). The powders were mixed as a slurry in 2-propanol for 24 h in a planetary ball mill, using zirconia balls in a polypropylene container. After drying, the softly agglomerated powder was crushed and sieved through a 60 mesh screen.

Hot pressing was then performed in nitrogen gas at 1 atm under uniaxial stress 30 MPa, at either 1570°C for 1 h, 1650°C for 1 h, or 1800°C for 3 h, followed by furnace cooling. These heat treatments produced the ''fine'' (*F*-Si_3N_4), ''medium'' (*M*-Si_3N_4), and ''coarse'' (*C*-Si_3N_4) microstructures described below.

(2) Microstructural Characterization

Specimen surfaces normal to the hot-press direction were polished to 1 μm finish to enable characterization. Figure 1 shows scanning electron microscopy (SEM) micrographs of the three materials. These surfaces were plasma etched to highlight the grain structures. No porosity is evident in the micrographs. Density determinations using the Archimedes method confirmed a porosity level <0.1% in each case. X-ray diffraction (XRD) was used to determine phase contents. Other specimens were immersed in hot hydrofluoric acid to dissolve the glassy phase, and the remnant silicon nitride grains collected on filter paper. SEM micrographs of these grains were analyzed digitally by computer by J. S. Wallace at NIST.

This characterization indicated the following microstructures:

(i) ''Fine'' (*F*-Si_3N_4, Fig. 1(a)), bimodal structure with ≈75 vol% equiaxed α grains of mean size ≈0.4 μm and ≈15 vol% elongated rodlike β grains of length 1.5 μm and diameter 0.4 μm, and with ≈10 vol% oxynitride glassy phase.[8]

(ii) ''Medium'' (*M*-Si_3N_4, Fig. 1(b)), bimodal structure with ≈20 vol% equiaxed α grains of mean size ≈0.5 μm and ≈70 vol% elongated rodlike β grains of length 4.0 μm and diameter 0.5 μm, again with ≈10 vol% glassy phase.

(iii) ''Coarse'' (*C*-Si_3N_4, Fig. 1(c)), elongated β grains of mean length ≈9 μm and diameter 1.5 μm, over a comparatively broad spread in grain size, and with ≈10 vol% glassy phase.

The SEM micrographs of each of these structures in Fig. 1 include surface traces of radial cracks from Vickers indentations. Cracking is predominantly intergranular in each case, the more so with increasing heterogeneity, attesting to the weakness of the boundaries. Bridging is observed along the crack paths, again more so in the coarser materials.[9,30] The well-behaved form of the crack traces in Fig. 1 confirms the suitability of Vickers indentations for toughness evaluations in the next subsection.

The Vickers indentations also provide an indication of hardness, determined here as $H = P/2a^2$, where *P* is peak load and *a* is impression half-diagonal. Values obtained (means ± standard deviations, five indentations at $P = 100$ N) are included

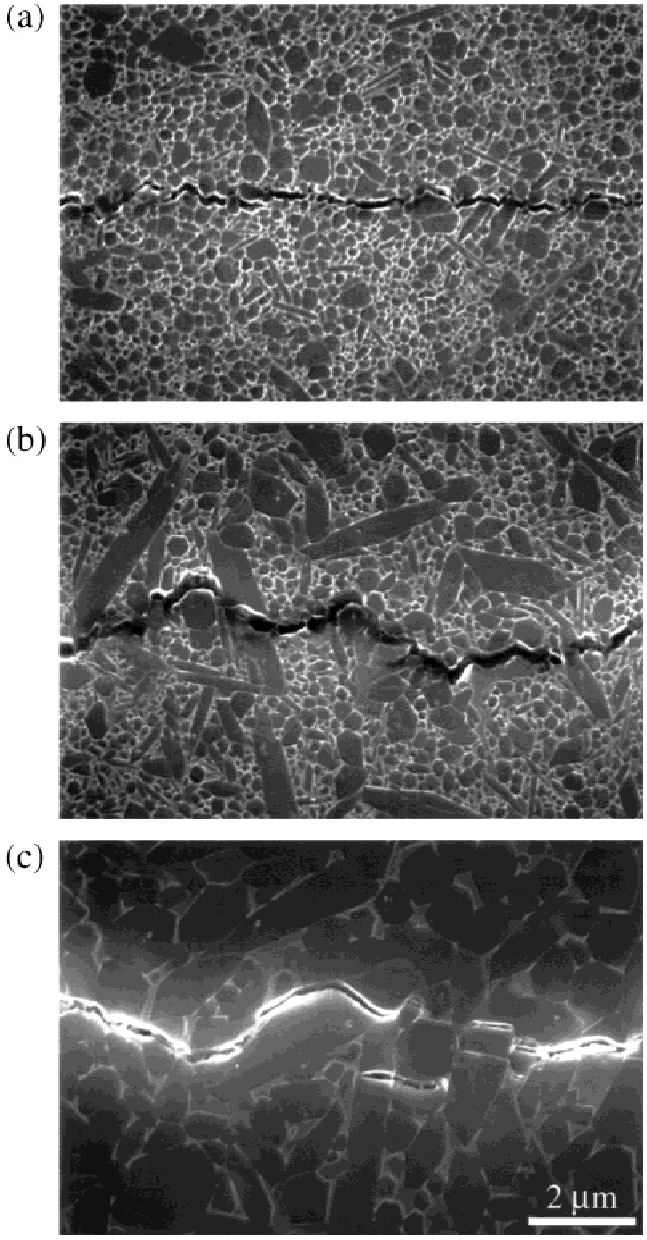

Fig. 1. SEM micrographs of silicon nitride specimens: (a) *F*-Si_3N_4, (b) *M*-Si_3N_4, (c) *C*-Si_3N_4. Specimens plasma etched for 40 s to reveal grain structures. Segments of radial cracks from Vickers indentations are visible. Note predominantly intergranular fracture, bridging in *C*-Si_3N_4.

in Table I. The monotonic decrease through $F \rightarrow M \rightarrow C$ correlates with the diminishing hardness of β phase relative to α phase.[3]

Young's modulus E and Poisson's ratio ν were independently determined for each material using routine sonic techniques.

(3) Strength and Toughness

Flexure specimens were prepared as bars 3 mm × 4 mm × 25 mm with polished surfaces and chamfered and polished edges, for strength and toughness evaluation. The flexure tests were made in four-point bending, inner span 10 mm and outer span 20 mm. Unless otherwise specified, these tests were made at fast loading rate (<20 ms break time) in ''inert'' environment (silicone oil), to minimize environmental effects.

The first bend tests were made on as-polished, unindented specimens, to establish a laboratory strength baseline for each silicon nitride type. Measured inert strengths (means ± standard deviation, 10 specimens) are shown in Table I.

Another set of bend tests was run on specimens after Vickers indentation, over a range of loads. Results representing breaks from indentations (means ± standard deviations, five specimens at each load) are plotted as the data points in Fig. 2. The baseline laboratory strengths for specimens without indentations are included as the shaded areas at left. The data set for F-Si_3N_4 is relatively low on the strength axis, with a slope close to −1/3 in logarithmic coordinates, indicative of a material with comparatively low, single-valued toughness. The data set for M-Si_3N_4 is higher, but again with slope close to −1/3, signifying an increased, but still close to single-valued, toughness. The data set for C-Si_3N_4 is highest at larger contact loads, but crosses below the M-Si_3N_4 curve at smaller loads; in C-Si_3N_4 the slope is significantly less than 1/3, indicating the existing of a rising crack resistance from the bridging constraints referred to in the preceding subsection. An objective deconvolution of the strength data in Fig. 2 using indentation fracture mechanics[31] yields the functional dependencies of toughness $K = K_R = T$ on crack size c shown in Fig. 3 (see Appendix for details). For F-Si_3N_4 and M-Si_3N_4, the toughness values are effectively constant, $T = T_0$ (grain boundary toughness), over the crack extension data range ≈40 to 700 μm. For C-Si_3N_4, $T(c)$ rises substantially over this same crack extension range.[13] Note again how the $T(c)$ curve for C-Si_3N_4 crosses below that for M-Si_3N_4 at low load, foreshadowing diminished short-crack properties (i.e., below $c \approx 100$ μm) in the former. Actual toughness values are indicated in Table I.

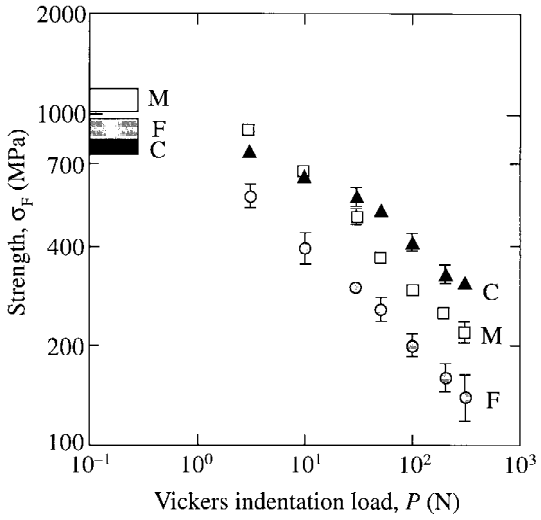

Fig. 2. Strength σ_F of Vickers-indented Si_3N_4 flexure specimens as function of indentation load P. Data for F-Si_3N_4 and M-Si_3N_4 closely follow classical relation $\sigma_F \propto P^{-1/3}$ for materials with single-valued toughness. Data for C-Si_3N_4 show flatter response, indicating rising toughness curve. Shaded areas at left indicate laboratory inert strengths for specimens without indentations.

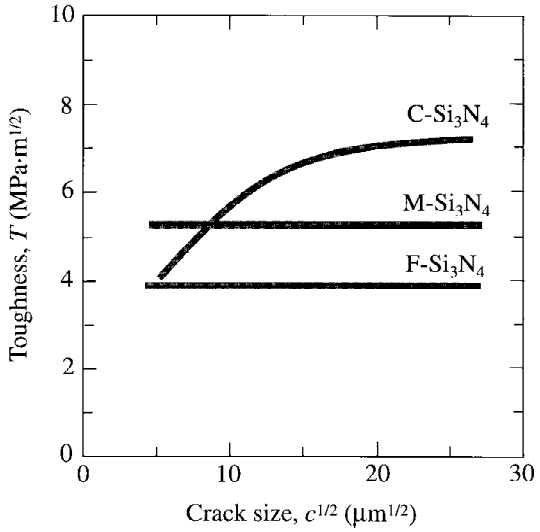

Fig. 3. Toughness curves of Si_3N_4 materials, deconvoluted from data in Fig. 2 (see Appendix).

With these evaluations we may estimate flaw sizes c_f from the base laboratory strengths σ_F (assuming the flaws to be initially in the stress-free state[32]). The slopes of the toughness curves in Fig. 3 are too small for any prefailure stable growth,[33] even for the C-Si_3N_4 material, so failure is expected to occur spontaneously when the applied stress-intensity factor K_A at the critical stress intersects the appropriate toughness curve $T(c)$,[10] i.e.

$$K_A = \sigma_F (\pi c_f)^{1/2} = T(c_f) \quad (1)$$

Estimates of c_f obtained in this way are included in Table I. Note in each case that the estimated flaw size is equivalent to a few grain dimensions.

III. Hertzian Contact Damage Tests

Hertzian damage tests were conducted to follow the evolution of damage in each of the F-Si_3N_4, M-Si_3N_4, and C-Si_3N_4 materials.[25] Indentations were made on diamond-polished surfaces (1 μm finish) using tungsten carbide (WC) spheres of radius $r = 1.21$–12.7 mm, to peak loads up to $P = 5000$ N and at a fixed crosshead speed 1.67 μm · s^{-1}. The indented surfaces were gold coated for examination by optical microscopy (Nomarski interference) and SEM.

(1) Indentation Stress–Strain Curves

Indentation stress–strain curves were evaluated from measurements of contact radius a (made visible by first coating the specimen surface with a gold film) at each given load P and sphere radius r.[18,19] Data representing indentation stress, $p_0 = P/\pi a^2$, as a function of indentation strain, a/r, are plotted in Fig. 4. The data for each material fall on a universal curve, independent of r, confirming geometrical similarity in the yield process.[27] The solid curves through the data are theoretical fits (Section IV). The inclined dashed line through the origin represents the limit for purely Hertzian elastic contacts on F-Si_3N_4[18,19] (Section IV). The horizontal dashed lines at upper right indicate hardness values for reference (Table I).

The indentation stress–strain curves in Fig. 4 deviate distinctly from linearity in the high stress region, indicating the onset of ''yield.'' Although the deviations are much less marked than in other, softer ceramics,[26] and despite the fact that part of the deviation is attributable to deformation in the WC indenters (the spheres were noticeably flattened by the contacts), a trend is discernible in the data. The nonlinearity is

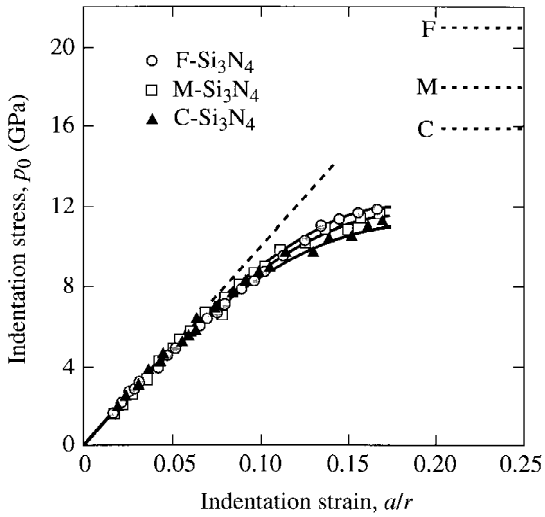

Fig. 4. Indentation stress–strain curves for Si_3N_4 materials, from Hertzian contact tests. Data plotted for range of sphere radius r = 1.21–12.7 mm (r values not distinguished). Solid curves are FEM-generated fits. Inclined dashed line through origin is Hertzian elastic limit for F-Si_3N_4. Horizontal dashed lines at upper right indicate Vickers hardness values.

slightest for the F-Si_3N_4, and greatest for the C-Si_3N_4, consistent with the observed tendency to softening with increasing microstructural heterogeneity.

(2) Damage Initiation: Critical Loads for Quasi-plasticity and Ring Cracking

Hertzian contact tests were conducted on polished surfaces of F-Si_3N_4, M-Si_3N_4, and C-Si_3N_4 specimens to characterize quasi-plasticity and ring crack damage types and to determine critical conditions for the onset of these damage modes. Indentation loads were incremented at successive contacts to determine the first signs of damage using Nomarski illumination: for yield, surface depression; for fracture, ring cracking. A useful adjunct in the detection of cracking was the use of an acoustic sensor mounted on the specimen surface close to the contact to monitor acoustic emissions during loading.[34,35]

Figure 5 shows surface views of residual contact sites on each of the silicon nitride materials after indentation with a WC sphere of radius r = 1.98 mm at peak load P = 4000 N, along with corresponding acoustic signal traces over a loading half-cycle. The distinctive damage patterns and acoustic signatures suggest a trend from fracture-dominated to deformation-dominated with increasing microstructural heterogeneity. In F-Si_3N_4 (Fig. 5(a)), the surface ring cracks are relatively pronounced and the acoustic signals strong, implying deep crack penetration. In this material, there is no sign of accompanying irreversible deformation, at least at this sphere radius. In M-Si_3N_4 (Fig. 5(b)), the ring cracks are less pronounced and the acoustic signals weaker, suggesting less crack penetration. A residual surface depression is now apparent within the ring crack, confirming the onset of quasi-plasticity. In C-Si_3N_4 (Fig. 5(c)), the ring cracks are even less distinct and the acoustic signals correspondingly very much weaker, suggesting even shallower surface fracture. In this case the surface depression within the ring cracks is strongly evident.

The acoustic spikes correlate one-to-one with the surface ring crack locations in Fig. 5, enabling more accurate determination of the critical loads for first ring cracking, P_C. From such correlations, the ratio of the surface ring-crack radius R_0 to critical contact radius a_C lies within the range $R_0/a_C \approx 1.15 \pm 0.05$ for all three silicon nitrides.[36] On the other hand, there is no indication of any correlation between the acoustic signal and the incidence of quasi-plasticity in the silicon nitrides, even in the comparatively deformable C-Si_3N_4. Weibull plots of P_C for sphere radius r = 1.98 mm in Fig. 6 (14 indentations) typify data variations.

Results of determinations of the threshold loads for yield, P_Y, and for ring cracking, P_C, are plotted as data points in Fig. 7 as a function of sphere radius r for each material. (The limited yield data range in the intrinsically brittle F-Si_3N_4 in Fig. 7(a) reflects the difficulty in detecting irreversible deformation in this material.) Solid curves are fits to the data (Section IV). Two trends are of interest:

(i) Effect of indenter size: The critical loads for onset of fracture and yield show different functional dependencies on sphere radius in all materials, implying a size effect in the competition between these two processes. The crossover point between $P_Y(r)$ and $P_C(r)$ signals a kind of ''ductile–brittle'' transition,[37–41] with a predilection toward yield at smaller sphere sizes (''sharp'' indenters) and toward fracture at larger sphere sizes (''blunt'' indenters).[42]

(ii) Effect of microstructure: The data crossover point occurs at ever-increasing sphere sizes with increasing microstructural heterogeneity, so that, over the size range covered, F-Si_3N_4 is relatively brittle and C-Si_3N_4 is relatively quasi-plastic, with M-Si_3N_4 intermediate. On an absolute load scale, values of P_Y decrease monotonically in the sequence $F \rightarrow M \rightarrow C$. This trend is consistent with the progressively diminishing Vickers hardness values in Table I. Values of P_C increase from F-Si_3N_4 to M-Si_3N_4; however, P_C decreases again, to its lowest level, in C-Si_3N_4. These trends in the fracture behavior correlate with the measured toughness characteristics in the short-crack region of Fig. 3.

(3) Damage Evolution: Development of Yield Zones and Ring Cracks

Bonded-interface specimens were used for section views through subsurface damage zones.[18,19] In each such specimen, two polished half-blocks were clamped face-to-face with an intervening thin layer of adhesive, and the top surface itself then polished. Indentations were made across the surface trace of the bonded interface, the adhesive subsequently dissolved in acetone, and the separated half-blocks gold coated for examination in Nomarski illumination.

Half-surface and section views of the contact damage obtained at r = 1.98 mm and P = 4000 N are shown in Fig. 8 (cf. Fig. 5). In F-Si_3N_4 (Fig. 8(a)), a fully developed subsurface cone crack is apparent.[42–44] Once beyond the initial surface ring, the cone crack propagates at an angle $\alpha \approx 19 \pm 2°$ to the top free surface. No accompanying deformation is detectable beneath the contact circle (cf. Fig. 5(a)). This kind of near-ideal brittle response is typical of homogeneous, fine-grain ceramics.[17] In M-Si_3N_4 (Fig. 8(b)), a cone crack is again evident, at approximately the same angle but considerably shorter in length. There is also now clear evidence of a subsurface quasi-plastic deformation zone, accounting for the slight surface depression (cf. Fig. 5(b)). The response is in an intermediate stage, with fracture and deformation in mutual competition. In C-Si_3N_4 (Fig. 8(c)), the incipient surface ring crack collars show virtually no penetration at all in the section view. The subsurface quasi-plastic zone, on the other hand, is considerably more intense, consistent with the pronounced surface depression (cf. Fig. 5(c)). This last response is typical of tough, but soft, heterogeneous ceramics,[26] with a macroscopic deformation zone geometry beginning to approach that of fully plastic metals.[27,45]

Figure 9 shows the progressive evolution of the subsurface damage zone with increasing load in the coarse C-Si_3N_4 material, again for r = 1.98 mm. Once more, damage initiates beneath the contact, where the shear stress is a maximum, and gradually progresses until the plastic zone is fully developed.[26] Note that the minimum load in this sequence, P = 1000 N (Fig. 9(a)), lies just above the yield threshold for spheres of this size (cf. Fig. 7(c)).[25] Figure 10, a higher-magnification SEM

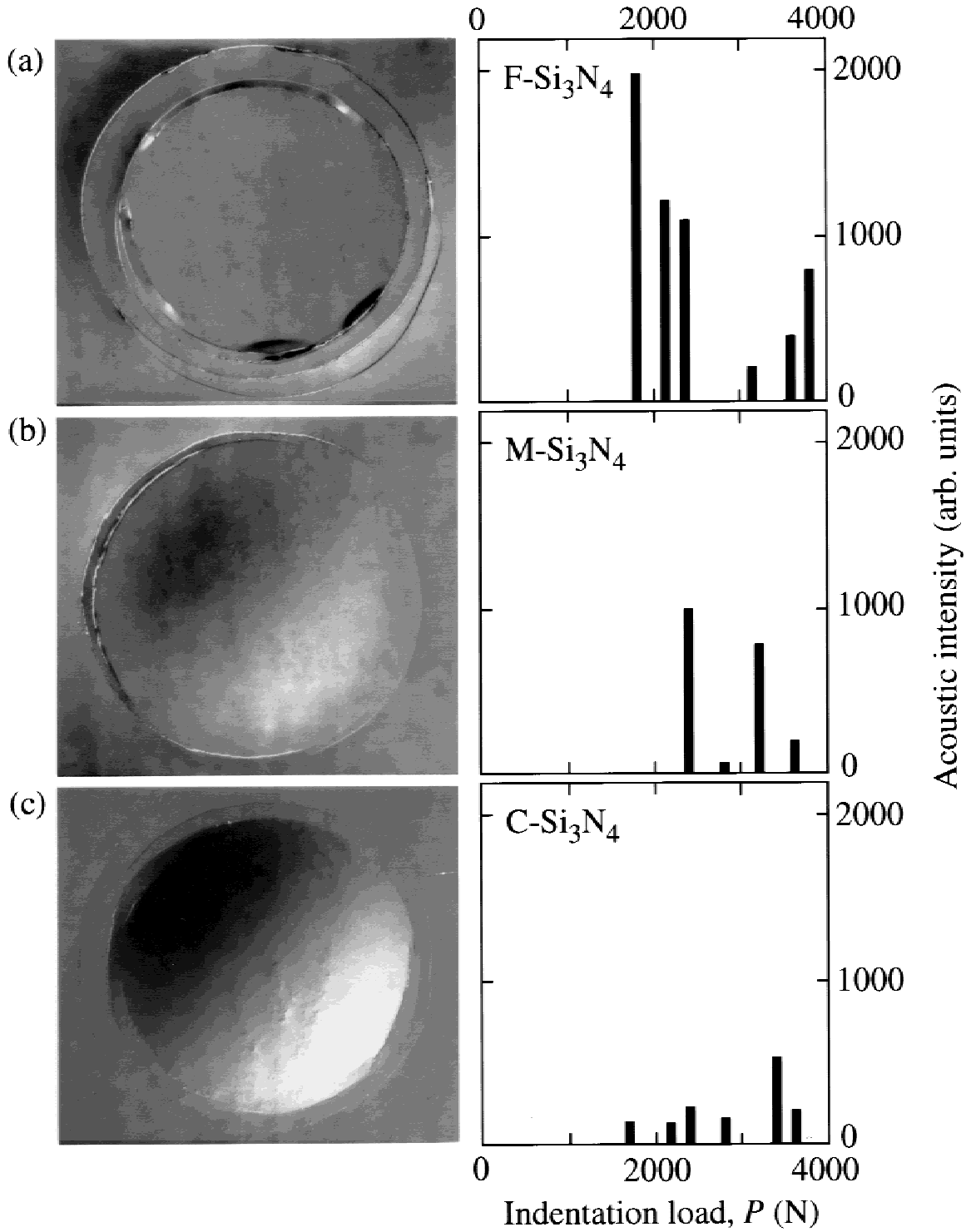

Fig. 5. Hertzian contact sites in (a) *F*-Si_3N_4, (b) *M*-Si_3N_4, (c) *C*-Si_3N_4, from WC sphere of radius $r = 1.98$ mm at load $P = 4000$ N. Left column: optical micrographs (Nomarski), showing surface views. Right column: corresponding acoustic emission signals, plotted as function of P over a loading half-cycle (acoustic signal in arbitrary units, but same scale in all cases). Acoustic spikes correlate with ring crack pop-in.

micrograph of the central subsurface damage zone from Fig. 9(e), reveals the underlying micromechanical form of the damage process in *C*-Si_3N_4.

Bonded-interface specimens like those in Figs. 8 and 9 allow for direct determination of characteristic dimensions of fully propagating ring cracks. Figure 11 shows data (closed symbols) for ring crack coordinates c and C, measured respectively from the surface ring or virtual cone tip to the cone base (see inset), as a function of peak load P, for $r = 1.98$ mm. As a check against the possibility of artifacts in the crack geometry from the bonding procedure, data from sections polished through contact centers *after* indentation on bulk specimens surfaces are included in Fig. 11 (open symbols). The trend to strongly diminishing crack sizes in the sequence $F \rightarrow M \rightarrow C$ noted in Fig. 8 is again in evidence. Solid curves represent data fits or predictions (Section IV).

The suppression of cone cracking noted in Fig. 8(c) warrants further attention, because of its pertinence to strength degradation (Part II). Comparative SEM images of the near-surface region for the extreme cases *F*-Si_3N_4 and *C*-Si_3N_4 are shown in

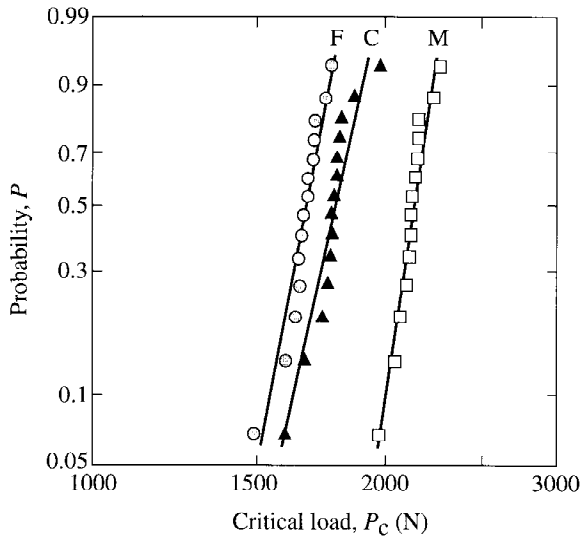

Fig. 6. Weibull diagrams plotting critical load for ring crack pop-in for silicon nitride materials, using WC spheres of radius $r = 1.98$ mm. The fits correspond to Weibull moduli: for *F*-Si_3N_4, $m = 19$; for *M*-Si_3N_4, $m = 28$; for *C*-Si_3N_4, $m = 22$.

Fig. 12. Although a common intergranular mode of fracture is again evident (cf. Fig. 1), the crack growth is more highly deflected in the coarse-grain *C* material (consistent with observations of enhanced crack path disruption in heavily bridged ceramics[9,46]). This enhanced tortuosity is more apparent in the higher-magnification micrograph in Fig. 13. It is noteworthy that the scale of the grain facet deflections in the C material (Figs. 12(b) and 13) is comparable with the depth of the surface ring collar in the *F* material (Fig. 12(a)).

IV. Mechanics

In order to analyze the contact damage patterns in the different silicon nitride materials it is necessary to evaluate the contact fields. Because of the quasi-plasticity component we resort to a numerical algorithm, using finite element modeling (FEM), details of which are described elsewhere.[26] First, we match the *indentation* stress-strain curves, $p_0(a/r)$ (Fig. 4), with constitutive *uniaxial* compression stress–strain responses, $\sigma(\epsilon)$, to establish a condition for deformation. Then we map principal shear components, for evaluation of the quasi-plastic yield zones, and principal tensile components, for evaluation of the ring cracks.

(1) FEM and Elastic–Plastic Contact Fields

The FEM algorithm assumes a WC sphere of specified radius r in normal frictionless contact with a flat Si_3N_4 specimen surface. Deformation in both WC and Si_3N_4 above the respective elastic limits is governed by a critical shear stress yield criterion, in accordance with idealized uniaxial compression stress–strain functions $\sigma(\epsilon)$. Such functions are plotted in Fig. 14: for WC (dashed line), from a previous calibration;[26] for Si_3N_4 (solid lines), constructed from the following input parameters:

(i) Young's modulus E and Poisson's ratio ν (Table I), determining the slope in the initial elastic region. This initial linear region corresponds to an equivalent initial linear region in the indentation stress–strain curve, determined by the Hertzian relation $p_0 = (3E/4\pi k)a/r$ ($k \approx 0.81$ for WC/Si_3N_4).[28]

(ii) Yield stress Y, determining the quasi-plasticity cutoff point. Quasi-plasticity is predicted to activate when the maximum shear stress $\approx 0.47p_Y$ in the Hertzian contact field (located at a depth $\approx 0.5a$ below the contact center) attains $Y/2$, corresponding to a point of deviation $p_Y = P_Y/\pi a^2 \approx 1.1Y$ on the indentation stress–strain curve.[27,47] Observations of the critical

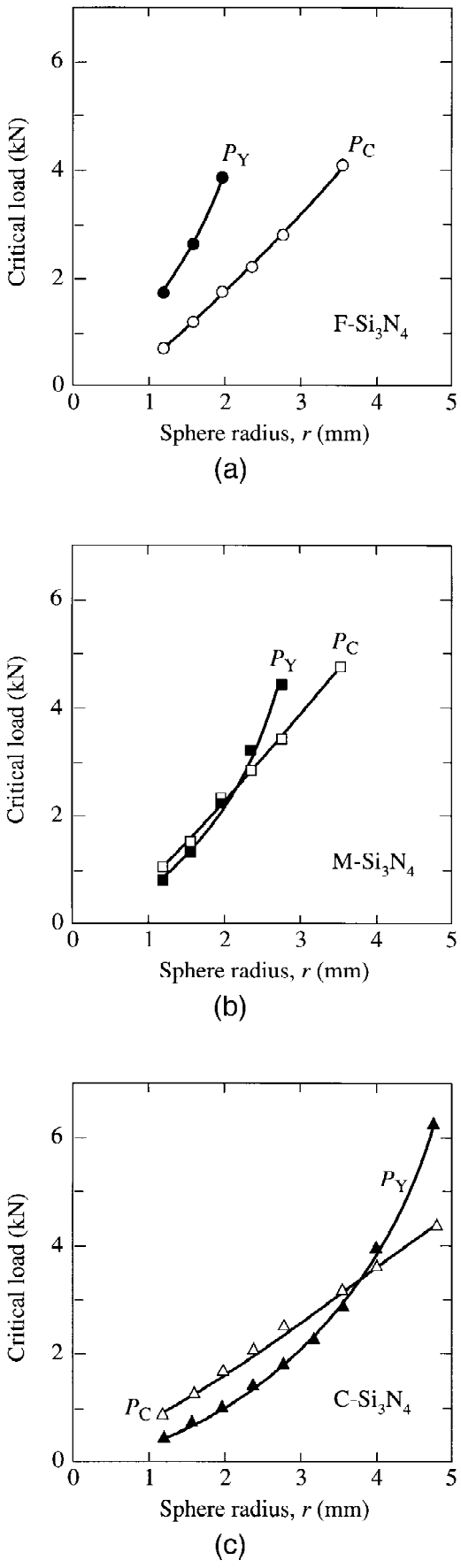

Fig. 7. Mean critical contact load for ring crack initiation, P_C, and yield, P_Y, as function of WC sphere radius r, for (a) *F*-Si_3N_4, (b) *M*-Si_3N_4, (c) *C*-Si_3N_4. Note different dependencies of P_C and P_Y on r, and diminishing P_Y/P_C through $F \rightarrow M \rightarrow C$. Solid curves through $P_Y(r)$ data are theoretical fits, through $P_C(r)$ data are empirical fits.

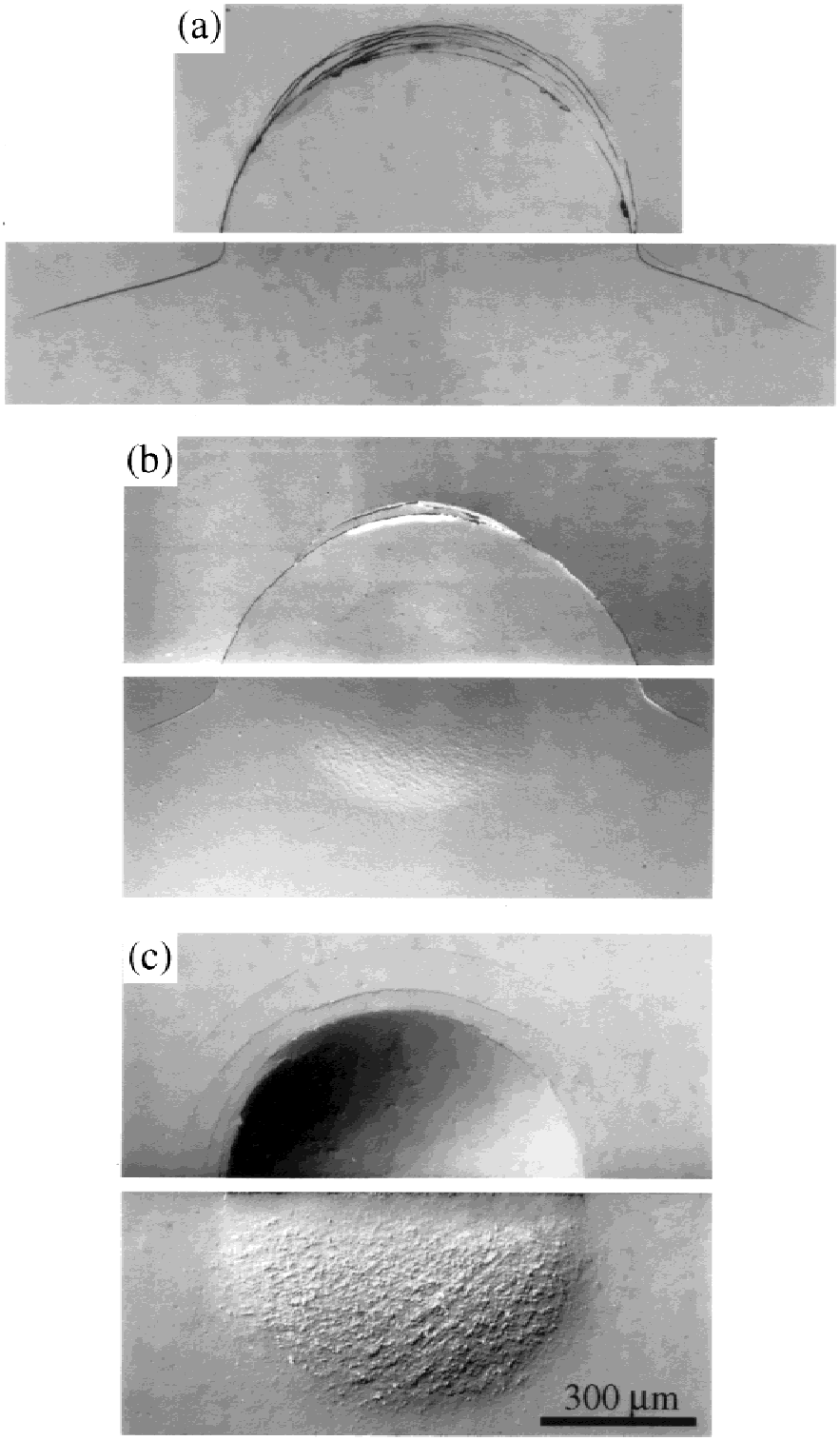

Fig. 8. Half-surface and side views of Hertzian contact damage in (a) *F*-Si_3N_4, (b) *M*-Si_3N_4, (c) *C*-Si_3N_4, from WC sphere radius $r = 1.98$ mm at load $P = 4000$ N. Nomarski optical micrographs of bonded-interface specimens. Note transition from fracture-dominated to quasi-plasticity-dominated damage pattern through $F \rightarrow M \rightarrow C$.

loads (Fig. 7) and corresponding contact radii at first permanent impression enable determination of Y (mean values included in Table I).

(iii) Strain-hardening coefficient α_0, determining the slope $(\sigma - Y)/(\epsilon E - Y)$ in the (assumed) linear quasi-plastic region.[26] The coefficient α_0 is adjusted for each material to provide a best fit to the indentation stress–strain data in this region (values included in Table I).

In the actual FEM computations the load P is increased incrementally, and the contact radius a computed at each step, allowing for computation of indentation stresses ($p_0 = P/\pi a^2$) and indentation strains (a/r). The indentation stress–strain functions regenerated in this way, with due allowance in the algorithm for deformation in the WC sphere,[26] are plotted in Fig. 4 (solid curves), along with the Hertzian elastic limit for *F*-Si_3N_4 (dashed line). The regenerated curves fit the data within the experimental scatter. Note that whereas the indentation stress–strain curves in Fig. 4 show significant deviations

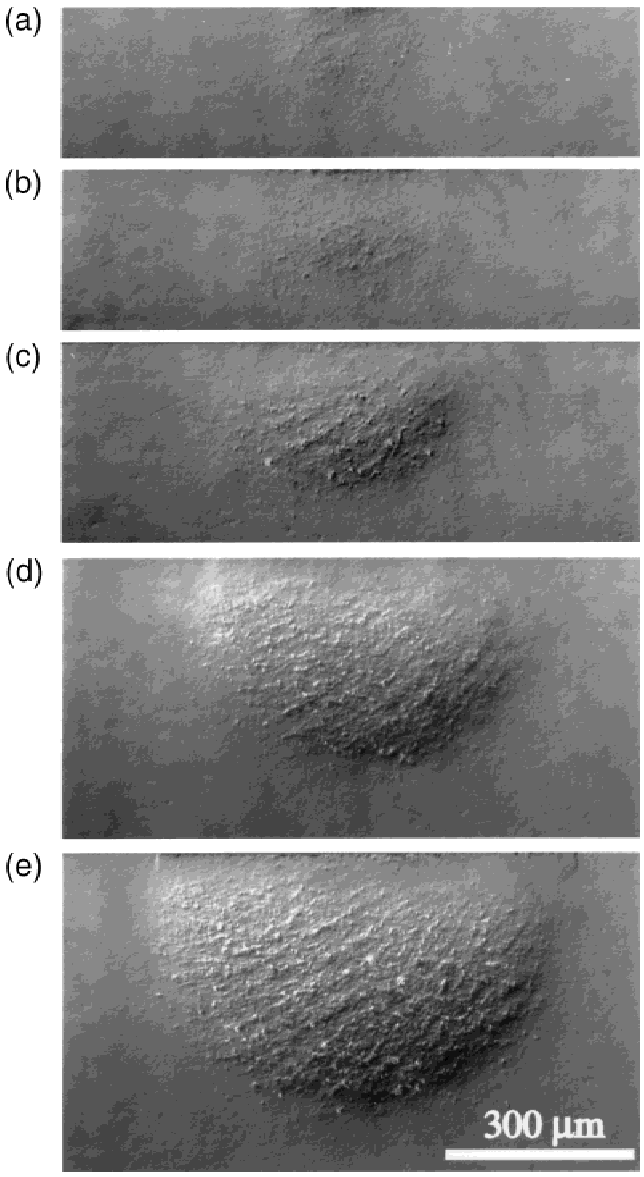

Fig. 9. Half-surface and side views of Hertzian contact damage in C-Si_3N_4, from WC sphere radius $r = 1.98$ mm, at loads (a) $P = 1000$, (b) 1500, (c) 2000, (d) 3000, and (e) 4000 N. Nomarski optical micrographs of bonded-interface specimens.

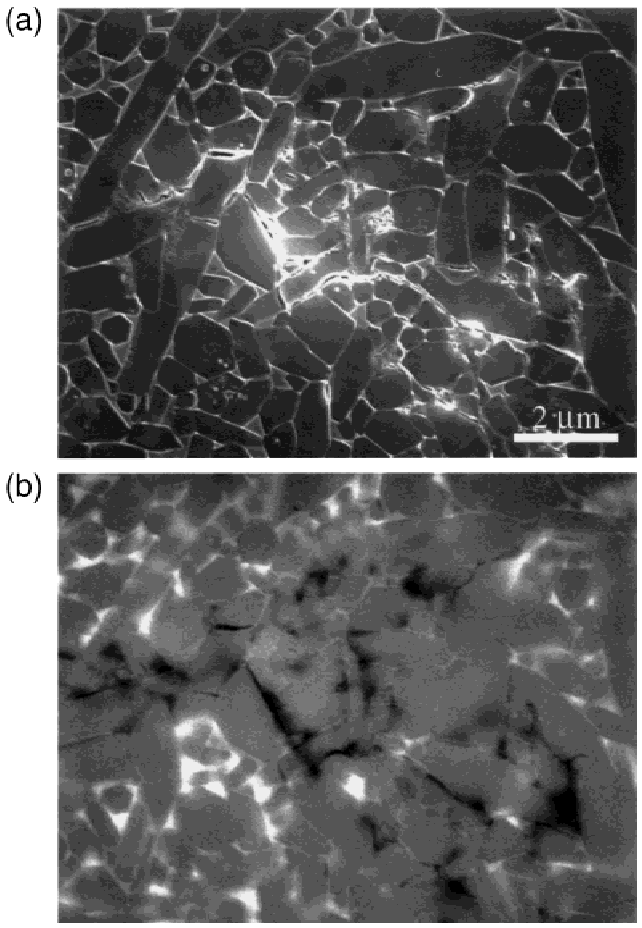

Fig. 10. SEM views of micromechanical damage from central region of Fig. 9(e): (a) secondary electrons, (b) backscattered electrons.

from linearity, these deviations are not much greater for M-Si_3N_4 and C-Si_3N_4 than for F-Si_3N_4. On the other hand, the intrinsic $\sigma(\epsilon)$ functions in Fig. 14 show marked material-to-material variations. This implies that the nonlinearities in the indentation data in Fig. 4 come in large part from deformation of the indenter, consistent with the relative location of the WC $\sigma(\epsilon)$ curve in Fig. 14 and the observed sphere flattening in Section III(1).

With these parametric ''calibrations,'' the FEM algorithm enables determination of contours and trajectories of maximum principal shear and tensile stresses ($\tau_{31} = \frac{1}{2}(\sigma_3 - \sigma_1)$ and $\sigma_1 \geq 0$), and corresponding strains (ϵ_{31} and ϵ_1) (with principal stresses defined such that $\sigma_1 \geq \sigma_2 \geq \sigma_3$ within the damage zone, and with σ_2 a ''hoop stress'').[26] These evaluations afford predictions of the quasi-plasticity zone boundaries, delineated by the yield condition $\tau_{31} = Y/2$,[26] and prospective crack paths, delineated by the σ_2–σ_3 trajectory surface.[44] In determining such contours and trajectories an internode interpolation procedure is used in the algorithm to smooth out grid discreteness.

(2) Quasi-plasticity

An analysis can be made of the effect of indenter size on critical load, $P_Y(r)$ in Fig. 7, using the principle of geometrical similarity. This principle states that, for isotropic homogeneous bodies, the stress and strain states are determined exclusively by *geometry* and not by *size* of the contact. The validity of this simple but powerful principle in contact mechanics has long been acknowledged.[27,48] One confirmation is the independence of Hertzian indentation stress–strain curves on sphere radius (Fig. 4). Another is the independence of yield stress on characteristic test dimension, in this case sphere radius r (a proviso being that r remains large compared with the scale of the microstructure, but small compared with the scale of the specimen). Accordingly, taking $p_Y = P_Y/\pi a^2 = 1.1Y$ from the previous subsection in conjunction with the Hertzian relation $a^3 = 4kPr/3E$,[48,49] we have

$$P_Y/r^2 = (1.1\pi Y)^3(4k/3E)^2 = \text{constant} \qquad (2)$$

so that, since Y is independent of r, the function $P_Y(r)$ is parabolic. The solid curves in Fig. 4 generated from Eq. (2) using E and Y (Table I) and $k \approx 0.81$ (WC/Si_3N_4) pass through the appropriate data sets, validating the similitude principle, at least over the data range.

Consider now the geometry of the quasi-plasticity damage zones. In Fig. 15 we plot FEM-computed contours of maximum principal shear strain for each Si_3N_4, at $r = 1.98$ mm and $P = 4000$ N, to facilitate direct comparisons with the section observations in Fig. 8. Contours of *strain* rather than *stress* are plotted in this instance to afford a stronger correlation with the observed damage intensity in the micrographs (bearing in mind that the Nomarski contrast used in Fig. 8 is displacement-

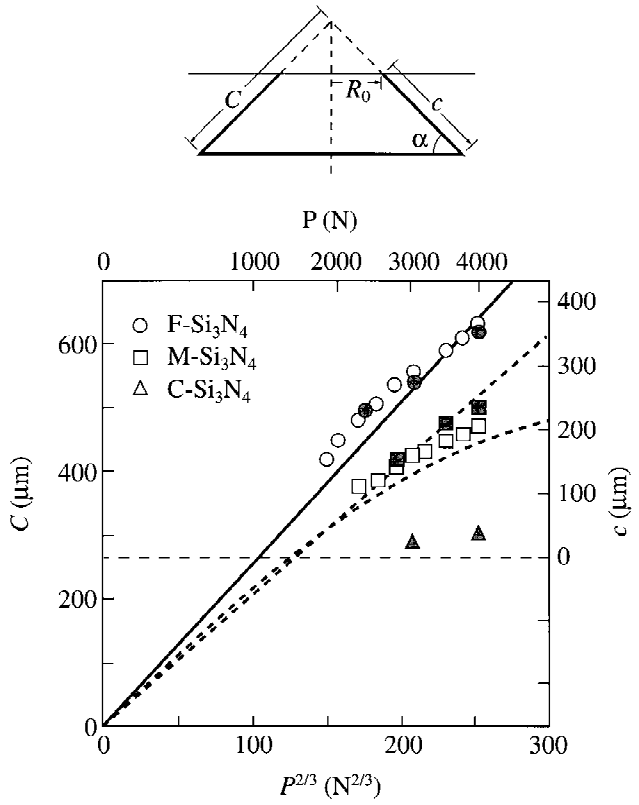

Fig. 11. Plot of Hertzian ring dimensions *c* of ring cracks as function of indentation load *P* for Si_3N_4 materials, WC sphere radius $r = 1.98$ mm. Open symbols from bonded-interface specimens, closed symbols from post-indentation-sectioned specimens. Solid curve through *F*-Si_3N_4 data is theoretical fit; dashed curves through *M*-Si_3N_4 and *C*-Si_3N_4 data are ensuing predictions.

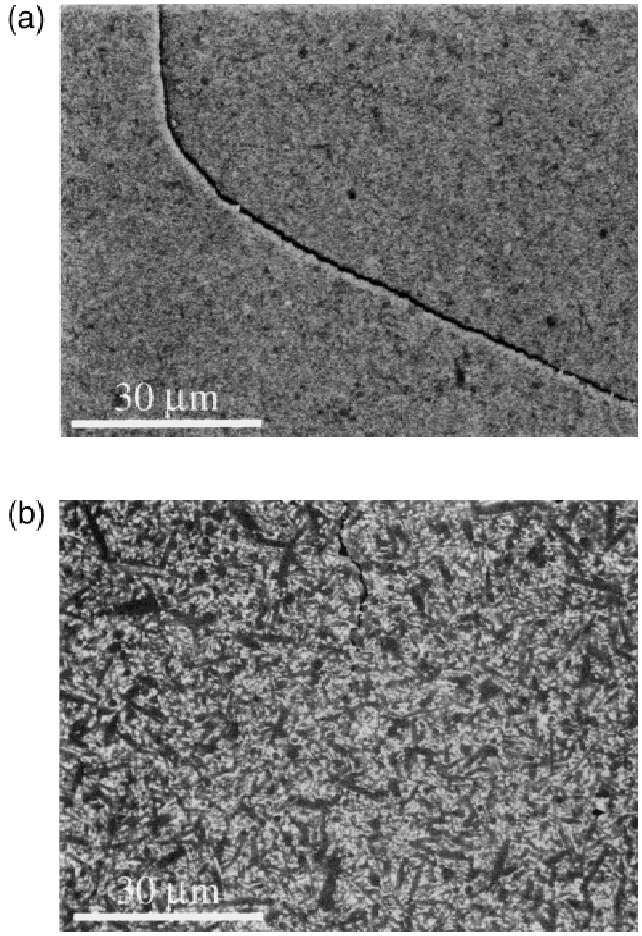

Fig. 12. SEM detail of ring crack path near region of surface initiation in (a) *F*-Si_3N_4 and (b) *C*-Si_3N_4, from WC sphere radius $r = 1.98$ mm at load $P = 4000$ N.

sensitive). Accordingly, the degree of shading in Fig. 15 indicates the levels of strain within the predicted yield zones: *F*-Si_3N_4, strain buildup, but a barely perceptible yield zone; *M*-Si_3N_4, moderate strain buildup within a modest yield zone; *C*-Si_3N_4, much more intense strain buildup within a larger yield zone. These computed characteristics are seen to correlate with the observations in Fig. 8.

Figure 16 shows a sequence of computed yield zone boundaries as a function of increasing load for *C*-Si_3N_4, at $r = 1.98$ mm, for comparison with Fig. 9.[26] This sequence indicates the evolutionary development of the quasi-plastic zone, from its initiation just above the critical load (Fig. 16(a)), through its intermediate confined expansion (Figs. 16(b–d)) to its nearly full development (Fig. 16(e)). Again, the predictions correlate with the observations in Fig. 9.

(3) Ring Cracks

A rich literature exists on the mechanics of Hertzian fracture.[10,36,42–44,50–61] The FEM-generated tensile stress fields that are assumed to control the crack evolution are plotted in Fig. 17 for each Si_3N_4, at $r = 1.98$ mm and $P = 4000$ N (cf. Fig. 8). In these figures solid curves are contours of principal stress σ_1, with shading indicating tensile regions. Extreme concentrations of tension in the near-surface regions outside the contact circle, where the ring cracks occur, are apparent. Note that the tensile field does not appear to vary as markedly from material to material as does the shear field in Fig. 15, indicating that relaxation effects outside the quasi-plastic damage zone are not strong (at least at the present contact conditions[26]). Dashed curves in Fig. 17 are σ_3 stress trajectories within the plane of the diagram (i.e., normal to σ_1 and contained within the plane of the diagram), indicating favored directions for the propagating cone cracks.

However, even in ideal, homogeneous solids, analytical fracture mechanics has proved somewhat limited in its capacity to deal with the highly complex ring crack evolution during Hertzian indentation. For instance, whereas the apparent correspondence between σ_3 trajectories and ensuing cone cracks has long been recognized,[44] leading to the presumption that the fracture mechanics may be completely predetermined by the prior Hertzian stress field, the angle $\alpha \approx 26°$ that the trajectories make with the top free surface in Fig. 17 is significantly larger than the $\alpha \approx 19°$ observed experimentally in Fig. 8. Such discrepancies in crack angle have been previously noted, and provisionally attributed to uncertainties in Poisson's ratio.[60,62] Only recently has it been demonstrated, using an FEM code that allows piecewise ring crack extension within the *evolving* (as distinct from the *prior* field),[63] that the stress trajectories are not an accurate determinant of the ultimate path, and that the fracture mechanics may differ quantitatively (if not qualitatively) from conventional calculations.

The rising toughness curves (Fig. 3) accompanying quasi-plasticity zones (Figs. 8 and 9) and exaggerated crack deflections (Figs. 12 and 13) that characterize the tough, heterogeneous ceramics of interest here add further to these difficulties. Consideration of the Hertzian contact problem in such heterogeneous materials is only now being addressed.[26] Accordingly, we confine ourselves to a phenomenological approach below:[64]

(A) Crack Propagation: We begin with the less complicated case of well-developed cone cracks. In their fully developed form, i.e., $C >> R_0/\cos\alpha$ (inset, Fig. 10), the ring cracks assume a geometry approaching that of a truncated cone. In the limit, the stress-intensity factor has the simple form for essentially pennylike cracks, $K(P,C) = \chi P/C^{3/2}$.[10,42] At increasing load, the cones propagate in stable equilibrium at $K(P,C) =$

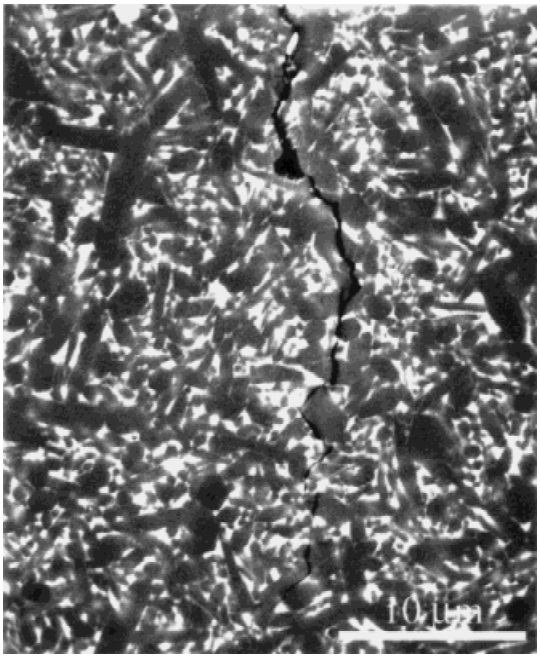

Fig. 13. Higher magnification view of ring crack collar region in C-Si_3N_4 in Fig. 12(b).

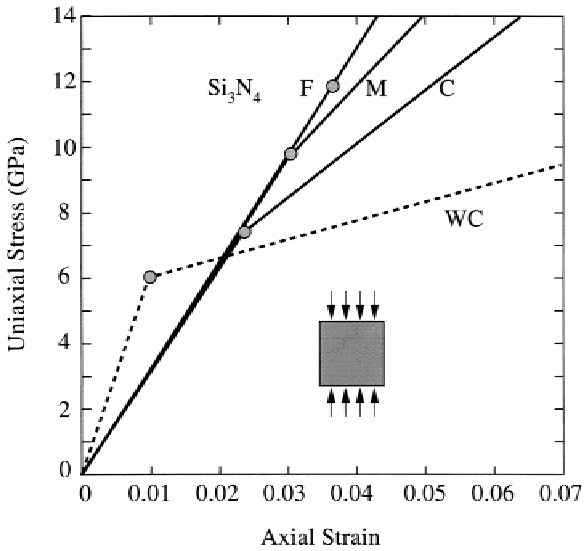

Fig. 14. Intrinsic stress–strain functions for uniform uniaxial loading state (inset): F-Si_3N_4, M-Si_3N_4, and C-Si_3N_4 (solid lines); WC indenter material (dashed line, from Ref. 26).

$T(C)$. For the special case of materials with constant toughness, $T = T_0 =$ constant (F-Si_3N_4 and M-Si_3N_4), we have a familiar result[10]

$$P/C^{3/2} = T_0/\chi = \text{constant} \tag{3}$$

where $\chi = \chi(\alpha)$ is a geometric coefficient.[10,43] In Fig. 11, using T_0 from Fig. 3, we have fitted this function asymptotically to the F-Si_3N_4 data to obtain $\chi = 0.0154$ (solid curve). Taking this as a baseline calibration, we have then predicted $P(C)$ for the other two materials (dashed curves): for M-Si_3N_4, using Eq. (3); and for C-Si_3N_4, using $\chi P/C^{3/2} = T(C)$. The predicted crack sizes C for M-Si_3N_4 are within ≈10% of the data points in the asymptotic region, which is about as good an agreement as may be expected for a material in which the cone cracks barely meet the condition ($C >> R_0/\cos\alpha$) for well-developed cracks (see Fig. 8(b)). The predicted sizes for C-Si_3N_4, on the other hand, are much higher than observed (in coordinate c, by more than an order of magnitude). The implication is that the cracks in C-Si_3N_4 remain entrapped within the initiation stage.

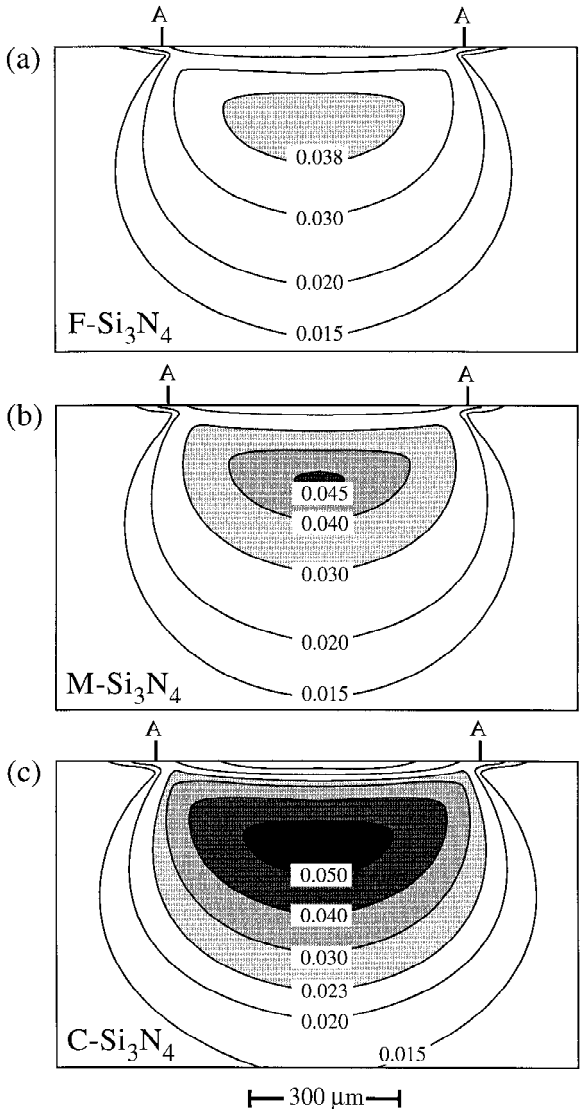

Fig. 15. FEM-generated contours of maximum principal shear strain, ϵ_{31}, for indentations with WC sphere, $r = 1.98$ mm, $P = 4000$ N: (a) F-Si_3N_4, (b) M-Si_3N_4, (c) C-Si_3N_4 (cf. micrographs in Fig. 8). Shading indicates yield zone. Contact diameter AA.

(B) Crack Initiation: In their initial stages the ring cracks have a geometry more akin to a cylindrical collar, with crack depth $c << R_0$.[44] Under such small-crack conditions the field more resembles a state of plane strain, which might appear to simplify determination of the equilibrium stress-intensity factor $K(P,r,c) = Pf(r,c) = T(c)$.[10,42,44,58–60] However, computations of $f(r,c)$ are complicated by the uncommonly high stress gradients along the crack path, ever varying with the expanding contact radius. There is also the above-mentioned issue as to how accurately one may determine $K(P,r,c)$ from the prior Hertzian stress field[63] and the superposed complications from polycrystalline heterogeneity. From traditional Hertzian fracture analyses it may be concluded that the critical load at which the crack equilibrium becomes unstable will generally increase with sphere radius and toughness and diminish with starting flaw size, but in a much more complex manner than in uniform stress fields. For the sphere size dependence, $P_C(r)$, reality generally lies between two extremes of behavior:[10,42,44,58–60,65]

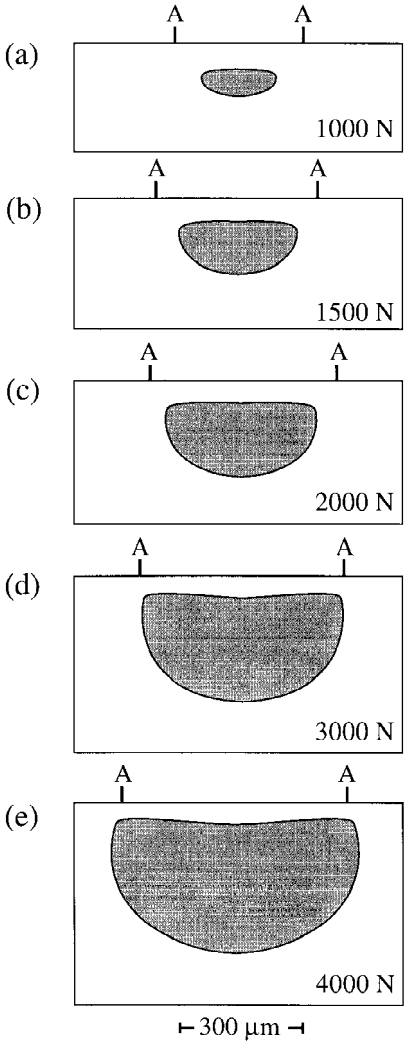

Fig. 16. FEM-generated yield zone boundary for indentation in heterogeneous silicon nitride with WC sphere, $r = 1.98$ mm, (a) $P =$ 1000, (b) 1500, (c) 2000, (d) 3000, and (e) 4000 N. Cf. micrographs in Fig. 9. Contact diameter AA.

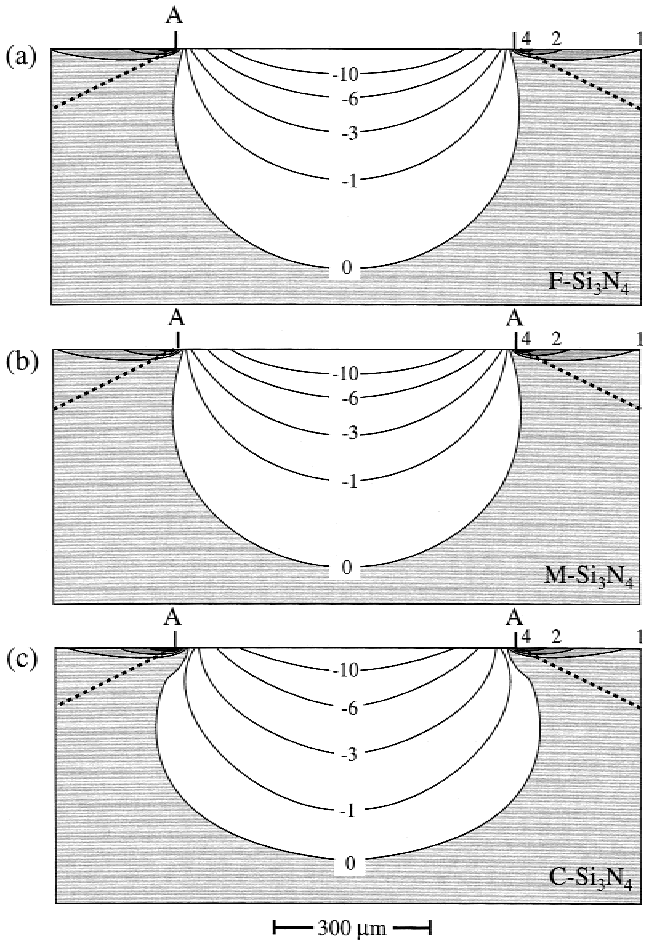

Fig. 17. FEM-generated contours of maximum principal normal stress σ_1, for indentations with WC sphere, $r = 1.98$ mm, $P = 4000$ N: (a) *F*-Si_3N_4, (b) *M*-Si_3N_4, (c) *C*-Si_3N_4 (cf. micrographs in Fig. 8). Shading indicates tensile zone. Dashed curves are σ_3 stress trajectories drawn from surface outside contact diameter AA.

(i) critical stress (small flaw, or large indenter) limit, where c_f is so small relative to R_0 that the stress inhomogeneity over its length may be neglected, so that criticality occurs when the maximum tensile stress exceeds the bulk strength of the material—in this limit the dependence is quadratic, $P_C/r^2 =$ constant, with dependence on c_f; (ii) ''Auerbach'' (large flaw, or small indenter) limit, where the stress inhomogeneity is so pronounced as to induce initial stable growth of the flaw to a critical depth prior to instability—in this limit the dependence is linear, $P_C/r =$ constant, independent of c_f. In Fig. 7 we simply note that the empirical curves through the data lie somewhere between these two limits, resulting in crossover with the $P_Y(r)$ curves. In the specific case of *C*-Si_3N_4, P_C may be interpreted as the load to produce a stably extending (entrapped) surface ring crack rather than an unstably propagating cone crack.

Again, the suppression of crack instability in *C*-Si_3N_4 warrants special attention. Recall the small differences in the tensile stress fields for the three Si_3N_4 materials in Fig. 17. This indicates that the crack suppression in *C*-Si_3N_4 must be due to some cause other than stress redistribution. As to material-related parameters, *C*-Si_3N_4 has the largest value of flaw size c_f (Section II(3)); and, in this crack-size region where instability might ordinarily be expected to occur, *C*-Si_3N_4 has the lowest toughness (Fig. 3). On these counts it should be *easier* to initiate full cone cracks in *C*-Si_3N_4 than in the other two Si_3N_4 materials. The contrary explanation appears to lie in the exaggerated intergranular crack deflections over the depth of the surface ring collar in Figs. 12 and 13. To quantify this point, let us hypothesize that the crack is constrained to propagate downward along a weak vertical planar boundary, instead of following the stress trajectory. (We choose the vertical path for simplicity—any other deviant planar path yields a similar result.) Figure 18 compares the falloff of FEM-generated radial stress σ_r (radial relative to the contact axis) along such a vertical path with that of the principal stress σ_1 along the stress trajectory path, for indentation conditions pertinent to Figs. 12 and 13. Whereas σ_1 remains wholly (if modestly) tensile along the entire crack path, σ_r quickly becomes compressive below ≈20 μm. The implication is that deviant ring cracks encounter compressive restraints, to a degree that scales with a characteristic grain dimension, resulting in premature crack entrapment in the more heterogeneous microstructures.

V. Discussion

In Part I of this study we have characterized Hertzian contact damage modes in silicon nitride in terms of microstructural heterogeneity. *Experimentally*, we have shown how the contact damage undergoes a transition from brittle fracture to quasi-plastic deformation as the Si_3N_4 grains grow larger and more elongate through the sequence $F \rightarrow M \rightarrow C$ (fine → medium → coarse) (Figs. 5 and 8). Attendant key elements of the microstructural development through this sequence are the fol-

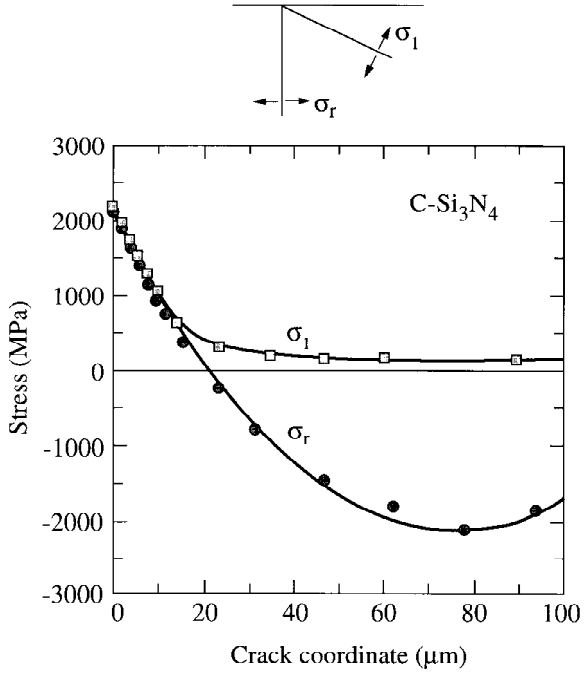

Fig. 18. FEM-generated normal stresses σ_1 along observed stress trajectory path and σ_r along hypothetically constrained vertical planar path for indentations with WC sphere, $r = 1.98$ mm, $P = 1750$ N, $R_0 = 360$ μm.

lowing: progressive transformation from α to β phase, known to simultaneously toughen and soften the silicon nitride structure;[3] progressive weakening of interphase boundaries between the Si_3N_4 grains and the glassy second phase, to simultaneously enhance the quasi-plasticity mode (Fig. 10) and suppress the fracture mode (Figs. 12 and 13).[16,25] *Theoretically*, we have used basic continuum mechanics concepts to interpret this ''brittle–ductile'' transition, with primary emphasis on the role of underlying microstructure (and indenter) scaling in the competition between the damage modes, but with reference also to conventional material parameters (toughness and strength, hardness and yield stress). FEM has been used as a means for evaluating the critical stress and strain components in the elastic–plastic contact zone: shear (Figs. 15 and 16), to account for the enhancement of quasi-plasticity in the coarser *C*-Si_3N_4 material; tension (Figs. 17 and 18), to account for the suppression of ring cracking.

It might ordinarily be thought that the quasi-plasticity mode in Si_3N_4 should be adequately quantifiable by the nonlinearities in externally measured indentation stress–strain (or load–displacement) responses, without the need for somewhat specialized (and time-consuming) ceramographic investigation. In softer ceramics, such responses show highly distinctive ''yield'' characteristics,[18,26] reminiscent of metals. However, although the indentation stress–strain data for our silicon nitrides (Fig. 4) do show a progressively increasing bendover through the sequence $F \rightarrow M \rightarrow C$, the deviations are comparatively slight. (Recall from Sections III(1) and IV(1) that part of this bendover is attributable to deformation of the indenting WC sphere. Recall also that the FEM algorithm contains inbuilt provision for separating out such artifacts.) This insensitivity to the onset of quasi-plasticity in the stress–strain data is perhaps a little surprising in view of the striking clarity of the developing yield zones in the micrographs (Figs. 8 and 9), reinforced by the FEM-generated shear strain contours (Fig. 15). The implication is that instrumented mechanical tests which monitor external load–displacement responses may not always be the most appropriate means for measuring (or even detecting) intrinsic quasi-plasticity components in relatively hard materials like silicon nitride.

It is of interest to explore how closely the threshold loads for the onset of quasi-plasticity and cracking damage in Hertzian contact relate to conventional macroscopic mechanical properties such as yield stress Y and strength σ_F, especially in light of the tendency for the $P_Y(r)$ and $P_C(r)$ data sets in Fig. 7 to cross each other (Section III(2)). We have already alluded to this crossover in terms of the well-documented transition to enhanced contact plasticity in otherwise brittle solids at smaller indenter sizes.[38–40] From the Hertzian relation for contact radius, $a^3 = 4kPr/3E$,[48,49] we may determine mean indentation pressure $p_0 = P/\pi a^2$ at any load in the elastic region, and thence maximum surface tensile stress, $\sigma = \frac{1}{2}(1 - 2\nu)p_0$ (at the contact circle), and subsurface shear stress, $\tau \approx 0.47p_0$ (at depth $\approx 0.5a$, Section IV(1)). This enables us to evaluate the critical stress at yield $Y = 2\tau_Y \approx 0.94p_Y$, and at ring cracking, $\sigma_C = \frac{1}{2}(1 - 2\nu)p_C$. Values of σ_C and Y evaluated in this way from the $P_Y(r)$ and $P_C(r)$ data in Fig. 7 are plotted in Fig. 19 as a function of sphere radius r. Included in Fig. 19 are the averaged yield stresses (Section III(2)) and bulk fracture strengths σ_F (Section II(3)). We see that the yield stress data are essentially independent of r, consistent with a size-independent hardness (at least over the sphere size range covered). The critical fracture stress data, on the other hand, decline steadily with r and, moreover, substantially exceed the bulk strengths over the entire data range. These are classical manifestations of fracture in highly inhomogeneous stress fields[10] and highlight the complete inadequacy of simplistic critical stress failure criteria in the general contact damage description. Finally, we note the uncommonly low ratio of maximum tension/shear, $\sigma/\tau \approx 0.25$ ($\nu \approx 0.27$), in the (predominantly triaxial compressive) Hertzian field, explaining why yield occurs readily below indentations but not in more conventional mechanical test specimens where significant tensile components are generally unavoidable.

The primary issue in this study is the role of microstructural heterogeneity in suppressing brittle fracture at the expense of quasi-plasticity. In *F*-Si_3N_4 (Fig. 8(a)) the ring cracks form into classical cones, with almost imperceptible subsurface quasi-plasticity. In *M*-Si_3N_4 (Fig. 8(b)) the ring cracks are still well formed, and propagate to sizes commensurate with the toughness (Fig. 11), despite modest attendant quasi-plasticity. In *C*-Si_3N_4 (Fig. 8(c)), however, the ring racks do not escape the near-surface region outside the contact circle (Figs. 12 and 13),

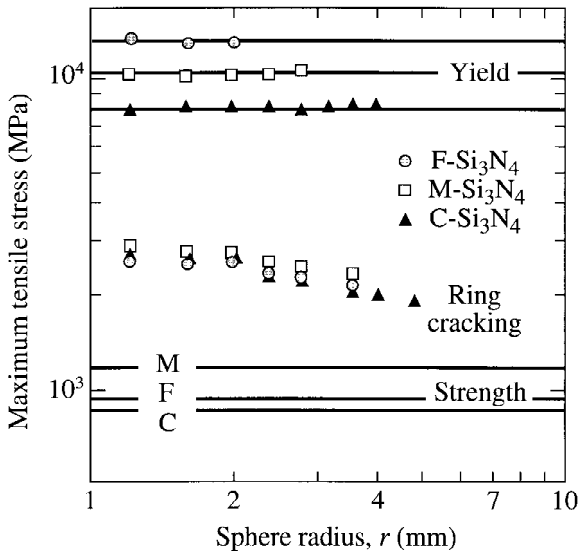

Fig. 19. Plot of threshold stresses $Y(r)$ for yield and $\sigma_C(r)$ for ring cracking. Individual points correspond to threshold load data from Fig. 7. Upper set of lines correspond to directly measured yield stresses (Section III(2)), lower set to measured bulk fracture strengths σ_F (Section II(3)). Whereas Y is essentially size-independent, σ_C declines with r, at levels substantially in excess of σ_F.

and quasi-plasticity dominates. We have argued (Section IV(3)) that the most likely cause of this entrapment is deflection of the ring crack along the weak interphase boundaries. It is generally true of contact fields that the principal tensile stress is much lower magnitude than the principal compression stress ($|\sigma_1| << |\sigma_3|$), so that any deviant crack becomes subject to a substantial restoring shear stress (mode II) (''directional stability'').[42] Whereas in fine grain structures these restoring forces are able to restore the crack path close to the ideal tensile stress trajectories, they are less able to do so in coarse materials. In the latter instance the crack is forced into a compression zone (Fig. 18) and becomes arrested in its incipiency.

A corollary to the previous discussion concerns the effect of starting flaw size c_f on the critical load P_C for ring cracking. We have mentioned the reduced sensitivity of the critical load to c_f as P_C becomes less quadratic and more linear with r, the more so as c_f increases, as a result of the contact field inhomogeneity (Section IV(3)). Microstructural coarsening may well reduce this sensitivity still further, by making it more difficult for the larger flaws to follow the stress trajectories. Hence in heterogeneous materials like *C*-Si_3N_4 especially large flaws, from either the microstructure or from spurious (e.g., abrasion) damage, may remain highly stable within the Hertzian field. There is a documented precedent for this anticipated ''damage tolerance,'' from Hertzian fracture data on glass surfaces with controlled abrasion flaws.[62]

The application in Section IV of established contact mechanics, supplemented by FEM, has enabled us to establish a phenomenological basis for quantifying the competition between yield and cracking in Hertzian fields. At the same time, we have acknowledged certain limitations in our mechanical descriptions, most strikingly in our capacity to account quantitatively for ring crack initiation in the highly heterogeneous *C*-Si_3N_4. Inadequacies of longstanding fracture mechanics approaches that use the prior Hertzian stress field to evaluate stress-intensity factors have been cited. The use of objective numerical procedures for computing such stress-intensity factors, allowing the crack to extend piecewise and reevaluating the crack-tip field at each step of the extension, would appear desirable,[63] especially when quasi-plasticity accompanies the fracture. Moreover, with greater microstructural heterogeneity the very notion of a single well-developed crack becomes increasingly suspect. In the limit of extreme heterogeneity, the damage is more properly described as a cloud of many microscopically localized microcracks (''shear faults'') (Fig. 10) than as a single macrocrack. Micromechanical modeling of the shear fault process itself remains in its infancy.[16,66–70] A basic understanding of how such shear faults respond collectively within the quasi-plastic damage zone is fundamental to any complete description of strength, wear, and fatigue in silicon nitrides and other ceramics.

The data and analysis presented in this study provide a basic starting point for the characterization and (ultimately) design of silicon nitride materials for bearing applications. Especially relevant in this context are the threshold load plots in Fig. 7. For any given bearing radius it would seem prudent to choose materials that avoid exceeding either P_Y or P_C in these diagrams. Over the radius range $r = 1$–4 mm covered in Fig. 7, the lower-bounding envelope of $P_Y(r)$ or $P_C(r)$ curves is highest for *M*-Si_3N_4. This would appear to provide sound justification for the choice of an intermediate-grade Si_3N_4 for bearing-grade material (Section 1). In this sense, Fig. 7 may be regarded as a kind of ''damage map'' for evaluating the prospective incidence of damage at any design bearing load P and radius r. It may be noted in Fig. 7 that quasi-plasticity is more likely to precede fracture as the bearing size is made smaller and the material tougher. Even though such quasi-plasticity may not always be readily detectible on the bearing surface from ordinary visual inspection (since it initiates subsurface), it can be far from benign. Once initiated, it is subject to accumulation with increased or repeated loadings, with potential for extensive material removal.[15,19,25,34,35,71,72]

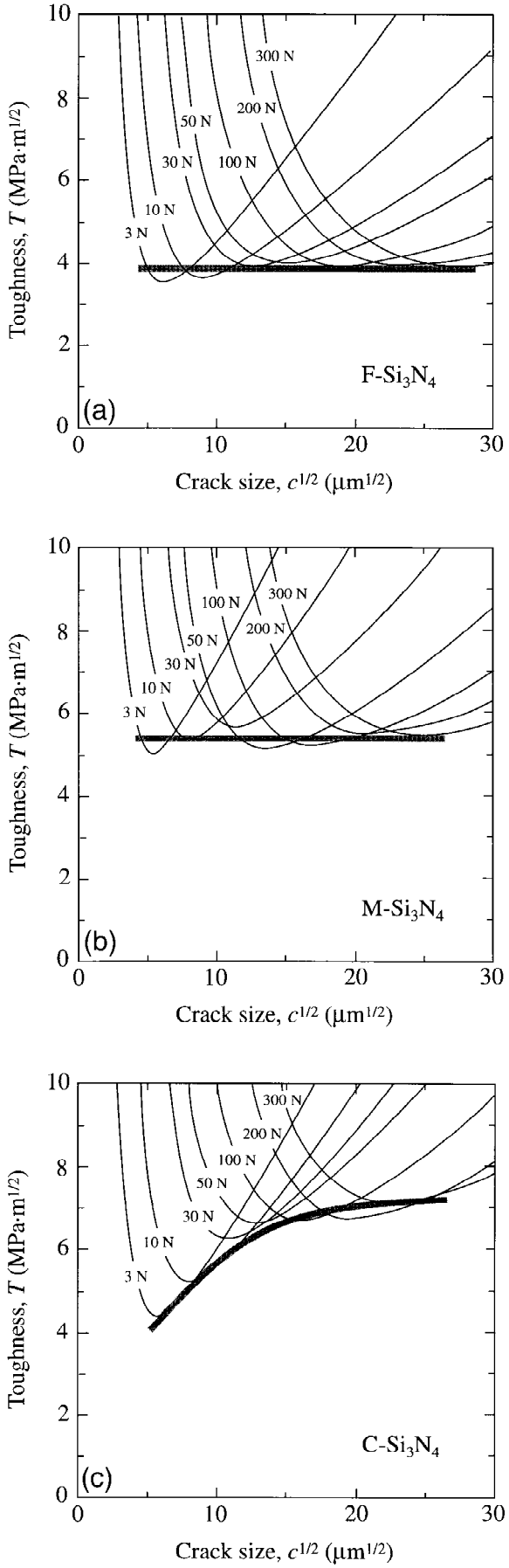

Fig. 20. Toughness-curve diagrams for (a) *F*-Si_3N_4, (b) *M*-Si_3N_4, (c) *C*-Si_3N_4. Families of solid curves are plots of $K'_A(c)$ in Eq. (A-1) using strength data from Fig. 2. Shaded lines are $T(c)$ functions, plotted as locus of tangency points to $K'_A(c)$ curves.

In Part II of this study we shall investigate the effect of the two damage modes on subsequent strength properties.

APPENDIX

Deconvolution of Toughness Curves from Vickers Indentation–Strength Data

We now describe in greater detail deconvolution of the Vickers indentation–strength data $\sigma_F(P)$ in Fig. 2 to generate the toughness curve $K_R = T(c)$ in Fig. 3. This is accomplished using an objective indentation–strength *K*-field protocol.[31] Under the action of an applied stress σ_A, radial cracks of size c produced at indentation load P extend according to an equilibrium condition

$$K'_A(c) = \psi\sigma_A c^{1/2} + \chi P/c^{3/2} = T(c) \quad \text{(A-1)}$$

where $K'_A(c)$ is a ''global'' applied stress-intensity factor, and ψ and χ are crack-geometry and residual-contact coefficients. For a given load P, failure occurs at the applied stress $\sigma_A = \sigma_F$ that satisfies the ''tangency condition''

$$dK'_A(c)/dc = dT(c)/dc \quad \text{(A-2)}$$

Given an appropriate calibration of the coefficients ψ and χ, we may generate families of $K'_A(c)$ curves from the $\sigma_F(P)$ data sets in Fig. 2. Toughness curves $T(c)$ may then be objectively determined as envelopes of tangency points to these families of curves.

Such constructions are made in Fig. 20 for the three silicon nitride ceramics, as follows:

(i) We note first that the indentation–strength data for *F*-Si_3N_4 in Fig. 2 closely satisfy the condition $\sigma_F \propto P^{-1/3}$ for a single-valued toughness, $T(c) = T_0 = \text{constant}$,[32] so this material affords a useful control. In the approximation that the Vickers crack geometry is material-independent, we may retain $\psi = 0.77$ from a previous calibration, on alumina.[31] Allowing for a dependence in the residual contact field on the average modulus-to-hardness ratio $(E/H)^{1/2} = (320\ \text{GPa}/18\ \text{GPa})^{1/2} = 3.90$ (Table I),[73] we evaluate $\chi = 0.066$ for *F*-Si_3N_4 from that same previous study. Thus, inserting $\sigma_A = \sigma_F$ at each value of P into Eq. (A-1) from the control indentation–strength data in Fig. 2, we generate the family of $K'_A(c)$ curves in Fig. 20(a). We see that the envelope of tangency points is indeed horizontal, confirming a single-valued toughness $T(c) = T_0 = 3.8\ \text{MPa} \cdot \text{m}^{1/2}$ for this material.

(ii) For the *M*-Si_3N_4 and *C*-Si_3N_4 materials we use the same values of ψ and χ, in the approximation of relatively invariant $(E/H)^{1/2}$. We then generate appropriate families of $K'_A(c)$ curves in Figs. 20(b) and (c), using the indentation–strength data in Fig. 2. The envelope of tangency points is still horizontal for *M*-Si_3N_4, although higher, corresponding to $T(c) = T_0 = 5.2\ \text{MPa} \cdot \text{m}^{1/2}$. For *C*-$Si_3N_4$, the envelope yields a distinctly rising $T(c)$ curve.

Acknowledgments: We thank R. Krause for assistance with the hot pressing, J. S. Wallace for the grain size and shape characterizations of our silicon nitride materials, and N. P. Padture, I. M. Peterson, and H. Xu for many discussions with other experimental aspects of this work. We also wish to acknowledge useful discussions with R. E. Collins and C. Kocer on the Hertzian fracture problem.

References

[1]R. N. Katz and J. G. Hannoosh, ''Ceramics for High Performance Rolling Element Bearings: A Review and Assessment,'' *Int. J. High Technol. Ceram.*, **1,** 69–79 (1985).

[2]J. W. Lucek, ''Rolling Wear of Silicon Nitride Bearing Materials''; ASME Paper No. 90-GT-165, pp. 1–7 in *Gas Turbine and Aeroengine Congress and Exposition*, Brussels, Belgium, 1990.

[3]F. F. Lange, ''Fracture Toughness of Si_3N_4 as a Function of the Initial α-Phase Content,'' *J. Am. Ceram. Soc.*, **62** [7–8] 428–30 (1979).

[4]C.-W. Li and J. Yamanis, ''Super-Tough Silicon Nitride with *R*-Curve Behavior,'' *Ceram. Eng. Sci. Proc.*, **10** [7–8] 632–45 (1989).

[5]C.-W. Li, D.-J. Lee, and S.-C. Lui, ''*R*-Curve Behavior and Strength of *In-Situ* Reinforced Silicon Nitride with Different Microstructures,'' *J. Am. Ceram. Soc.*, **75** [7] 1777–85 (1992).

[6]C.-W. Li, S.-C. Lui, and J. Goldacker, ''Relation Between Strength, Microstructure, and Grain-Bridging Characteristics in *In-Situ* Reinforced Silicon Nitride,'' *J. Am. Ceram. Soc.*, **78** [2] 449–59 (1995).

[7]P. F. Becher, S. L. Hwang, H. T. Lin, and T. N. Tiegs, ''Microstructural Contributions to the Fracture Resistance of Silicon Nitride Ceramics''; pp. 87–100 in *Tailoring of Mechanical Properties of Si_3N_4*. Edited by M. J. Hoffmann and G. Petzow. Kluwer Academic Publishers, Dordrecht, Netherlands, 1994.

[8]M. J. Hoffmann, ''Analysis of Microstructural Development and Mechanical Properties of Si_3N_4''; pp. 59–72 in *Tailoring of Mechanical Properties of Si_3N_4*. Edited by M. J. Hoffmann and G. Petzow. Kluwer Academic Publishers, Dordrecht, Netherlands, 1994.

[9]P. L. Swanson, C. J. Fairbanks, B. R. Lawn, Y.-W. Mai, and B. J. Hockey, ''Crack-Interface Grain Bridging as a Fracture Resistance Mechanism in Ceramics: I, Experimental Study on Alumina,'' *J. Am. Ceram. Soc.*, **70** [4] 279–89 (1987).

[10]B. R. Lawn, *Fracture of Brittle Solids;* Chs. 2, 7, and 8. Cambridge University Press, Cambridge, U.K., 1993.

[11]S. J. Bennison and B. R. Lawn, ''Role of Interfacial Grain-Bridging Sliding Friction in the Crack-Resistance and Strength Properties of Nontransforming Ceramics,'' *Acta Metall.*, **37** [10] 2659–71 (1989).

[12]S. J. Bennison, J. Rödel, S. Lathabai, P. Chantikul, and B. R. Lawn, ''Microstructure, Toughness Curves and Mechanical Properties of Alumina Ceramics''; pp. 209–33 in *Toughening Mechanisms in Quasi-Brittle Materials.* Edited by S. P. Shah. Kluwer Academic Publishers, Dordrecht, Netherlands, 1991.

[13]B. R. Lawn, N. P. Padture, L. M. Braun, and S. J. Bennison, ''Model for Toughness-Curves in Two-Phase Ceramics: I, Basic Fracture Mechanics,'' *J. Am. Ceram. Soc.*, **76** [9] 2235–40 (1993).

[14]N. P. Padture, J. L. Runyan, S. J. Bennison, L. M. Braun, and B. R. Lawn, ''Model for Toughness-Curves in Two-Phase Ceramics: II, Microstructural Variables,'' *J. Am. Ceram. Soc.*, **76** [9] 2241–47 (1993).

[15]N. P. Padture, C. J. Evans, H. H. K. Xu, and B. R. Lawn, ''Enhanced Machinability of Silicon Carbide via Microstructural Design,'' *J. Am. Ceram. Soc.*, **78** [1] 215–17 (1995).

[16]B. R. Lawn, N. P. Padture, H. Cai, and F. Guiberteau, ''Making Ceramics 'Ductile','' *Science*, **263,** 1114–16 (1994).

[17]F. Guiberteau, N. P. Padture, H. Cai, and B. R. Lawn, ''Indentation Fatigue: A Simple Cyclic Hertzian Test for Measuring Damage Accumulation in Polycrystalline Ceramics,'' *Philos. Mag. A*, **68** [5] 1003–16 (1993).

[18]H. Cai, M. A. Stevens Kalceff, and B. R. Lawn, ''Deformation and Fracture of Mica-Containing Glass-Ceramics in Hertzian Contacts,'' *J. Mater. Res.*, **9** [3] 762–70 (1994).

[19]F. Guiberteau, N. P. Padture, and B. R. Lawn, ''Effect of Grain Size on Hertzian Contact in Alumina,'' *J. Am. Ceram. Soc.*, **77** [7] 1825–31 (1994).

[20]N. P. Padture and B. R. Lawn, ''Toughness Properties of a Silicon Carbide with an *In-Situ*-Induced Heterogeneous Grain Structure,'' *J. Am. Ceram. Soc.*, **77** [10] 2518–22 (1994).

[21]A. Pajares, F. Guiberteau, B. R. Lawn, and S. Lathabai, ''Hertzian Contact Damage in Magnesia-Partially-Stabilized Zirconia,'' *J. Am. Ceram. Soc.*, **78** [4] 1083–86 (1995).

[22]H. Makino, N. Kamiya, and S. Wada, ''Strength Degradation of Si_3N_4 by Contact Stress,'' *J. Mater. Sci. Lett.*, **7,** 475–76 (1988).

[23]H. Makino, N. Kamiya, and S. Wada, ''Grain Size Effects of Si_3N_4 on Damage Morphology Induced by Localized Contact Stress''; pp. 229–34 in Proceedings of the 1st International Symposium on the Science of Engineering Ceramics. Edited by S. Kimura and K. Niihara. Koda, Aichi-Prefecture, Japan, 1991.

[24]H. Makino, N. Kamiya, and S. Wada, ''Effects of Grain Size of Hot-Pressed Silicon Nitride on Contact Damage Morphology and Residual Strength,'' *J. Am. Ceram. Soc.*, **74** [8] 2001–2004 (1991).

[25]H. H. K. Xu, L. Wei, N. P. Padture, B. R. Lawn, and R. L. Yeckley, ''Effect of Microstructural Coarsening on Hertzian Contact Damage in Silicon Nitride,'' *J. Mater. Sci.*, **30,** 869–78 (1995).

[26]A. C. Fischer-Cripps and B. R. Lawn, ''Stress Analysis of Contact Deformation in Quasi-Plastic Ceramics,'' *J. Am. Ceram. Soc.*, **79** [10] 2609–18 (1996).

[27]D. Tabor, *Hardness of Metals.* Clarendon, Oxford, U.K., 1951.

[28]M. V. Swain and B. R. Lawn, ''A Study of Dislocation Arrays at Spherical Indentations in LiF as a Function of Indentation Stress and Strain,'' *Phys. Status Solidi*, **35** [2] 909–23 (1969).

[29]A. C. Fischer-Cripps, ''Elastic–Plastic Behavior in Materials Loaded with a Spherical Indenter,'' *J. Mater. Sci.*, in press.

[30]Y.-W. Mai and B. R. Lawn, ''Crack-Interface Grain Bridging as a Fracture Resistance Mechanism in Ceramics: II, Theoretical Fracture Mechanics Model,'' *J. Am. Ceram. Soc.*, **70** [4] 289–94 (1987).

[31]L. M. Braun, S. J. Bennison, and B. R. Lawn, ''Objective Evaluation of Short-Crack Toughness-Curves Using Indentation Flaws: Case Study on Alumina-Based Ceramics,'' *J. Am. Ceram. Soc.*, **75** [11] 3049–57 (1992).

[32]D. B. Marshall, B. R. Lawn, and P. Chantikul, ''Residual Stress Effects in Sharp-Contact Cracking: II, Strength Degradation,'' *J. Mater. Sci.*, **14** [9] 2225–35 (1979).

[33]R. F. Cook and D. R. Clarke, ''Fracture Stability, *R*-Curves and Strength Variability,'' *Acta Metall.*, **36** [3] 555–62 (1988).

[34]N. P. Padture and B. R. Lawn, ''Contact Fatigue of a Silicon Carbide with a Heterogeneous Grain Structure,'' *J. Am. Ceram. Soc.*, **78** [6] 1431–38 (1995).

[35]A. Pajares, L. Wei, B. R. Lawn, and D. B. Marshall, ''Damage Accumulation and Cyclic Fatigue in Mg-PSZ at Hertzian Contacts,'' *J. Mater. Res.*, **10** [10] 2613–25 (1995).

[36]T. R. Wilshaw, ''The Hertzian Fracture Test,'' *J. Phys. D,* **4** [10] 1567–81 (1971).
[37]B. R. Lawn, T. Jensen, and A. Arora, ''Brittleness as an Indentation Size Effect,'' *J. Mater. Sci.,* **11** [3] 573–75 (1976).
[38]B. R. Lawn and D. B. Marshall, ''Hardness, Toughness, and Brittleness: An Indentation Analysis,'' *J. Am. Ceram. Soc.,* **62** [7–8] 347–50 (1979).
[39]K. E. Puttick, ''Energy Scaling, Size Effects and Ductile–Brittle Transitions in Fracture,'' *J. Phys. D,* **12,** L19–23 (1979).
[40]K. E. Puttick, M. A. Shahid, and M. M. Hosseini, ''Size Effects in Abrasion of Brittle Materials,'' *J. Phys. D,* **12,** 195–202 (1979).
[41]K. Puttick, ''The Correlation of Fracture Transitions,'' *J. Phys. D,* **13,** 2249–62 (1980).
[42]B. R. Lawn and T. R. Wilshaw, ''Indentation Fracture: Principles and Applications,'' *J. Mater. Sci.,* **10** [6] 1049–81 (1975).
[43]F. C. Roesler, ''Brittle Fractures Near Equilibrium,'' *Proc. Phys. Soc. London,* **B69,** 981 (1956).
[44]F. C. Frank and B. R. Lawn, ''On the Theory of Hertzian Fracture,'' *Proc. R. Soc. London,* **A299** [1458] 291–306 (1967).
[45]T. O. Mulhearn, ''The Deformation of Metals by Vickers-Type Pyramidal Indenters,'' *J. Mech. Phys. Solids,* **7,** 85–96 (1959).
[46]P. L. Swanson, ''Crack-Interface Traction: A Fracture-Resistance Mechanism in Brittle Polycrystals''; pp. 135–55 in Advances in Ceramics, Vol. 22, *Fractography of Glasses and Ceramics.* Edited by J. Varner and V. D. Frechette. American Ceramic Society, Columbus, OH, 1988.
[47]R. M. Davies, ''Determination of Static and Dynamic Yield Stresses Using a Steel Ball,'' *Proc. R. Soc. London,* **A197** [1050] 416–32 (1949).
[48]K. L. Johnson, *Contact Mechanics.* Cambridge University Press, London, U.K., 1985.
[49]S. Timoshenko and J. N. Goodier, *Theory of Elasticity.* McGraw-Hill, New York, 1951.
[50]H. Hertz, *Hertz's Miscellaneous Papers*; Chs. 5 and 6. Macmillan, London, U.K., 1896.
[51]F. Auerbach, ''Measurement of Hardness,'' *Ann. Phys. Chem.,* **43,** 61 (1891).
[52]V. R. Howes and S. Tolansky, ''Pressure Crack Figures on Diamond Faces: I. The Octahedral Face,'' *Proc. R. Soc. London,* **A230,** 287–93 (1955).
[53]V. R. Howes and S. Tolansky, ''Pressure Crack Figures on Diamond Faces: I. The Dodecahedral and Cubic Faces,'' *Proc. R. Soc. London,* **A230,** 294–301 (1955).
[54]F. C. Roesler, ''Indentation Hardness of Glass as an Energy Scaling Law,'' *Proc. Phys. Soc. London,* **B69** [433] 55–60 (1956).
[55]B. R. Lawn, ''Hertzian Fracture in Single Crystals with the Diamond Structure,'' *J. Appl. Phys.,* **39** [10] 4828–36 (1968).
[56]F. B. Langitan and B. R. Lawn, ''Effect of a Reactive Environment on the Hertzian Strength of Brittle Solids,'' *J. Appl. Phys.,* **41** [8] 3357–65 (1970).
[57]M. V. Swain, J. S. Williams, B. R. Lawn, and J. J. H. Beek, ''A Comparative Study of the Fracture of Various Silica Modifications Using the Hertzian Test,'' *J. Mater. Sci.,* **8** [8] 1153–64 (1973).
[58]R. Warren, ''Measurement of the Fracture Properties of Brittle Solids by Hertzian Indentation,'' *Acta Metall.,* **26** 1759–69 (1978).
[59]R. Mouginot and D. Maugis, ''Fracture Indentation Beneath Flat and Spherical Punches,'' *J. Mater. Sci.,* **20,** 4354–76 (1985).
[60]K. Zeng, K. Breder, and D. J. Rowcliffe, ''The Hertzian Stress Field and Formation of Cone Cracks: I, Theoretical Approach,'' *Acta Metall.,* **40** [10] 2595–600 (1992).
[61]B. R. Lawn, ''Friction Processes in Brittle Fracture''; pp. 137–65 in *Fundamentals of Friction: Macroscopic and Microscopic Processes.* Edited by I. L. Singer and H. M. Pollock. Kluwer Academic Publishers, Dordrecht, Netherlands, 1992.
[62]B. R. Lawn, T. R. Wilshaw, and N. E. W. Hartley, ''A Computer Simulation Study of Hertzian Cone Crack Growth,'' *Int. J. Fract.,* **10** [1] 1–16 (1974).
[63]C. Kocer and R. E. Collins, ''The Angle of Hertzian Cone Cracks,'' *J. Am. Ceram. Soc.,* in press.
[64]B. R. Lawn, S. M. Wiederhorn, and H. Johnson, ''Strength Degradation of Brittle Surfaces: Blunt Indenters,'' *J. Am. Ceram. Soc.,* **58** [9–10] 428–32 (1975).
[65]F. B. Langitan and B. R. Lawn, ''Hertzian Fracture Experiments on Abraded Glass Surfaces as Definitive Evidence for an Energy Balance Explanation of Auerbach's Law,'' *J. Appl. Phys.,* **40** [10] 4009–17 (1969).
[66]H. Horii and S. Nemat-Nasser, ''Compression-Induced Microcrack Growth in Brittle Solids: Axial Splitting and Shear Failure,'' *J. Geophys. Res.,* **90** [B4] 3105–25 (1985).
[67]H. Horii and S. Nemat-Nasser, ''Brittle Failure in Compression: Splitting, Faulting and Brittle–Ductile Transition,'' *Philos. Trans. R. Soc. London,* **319** [1549] 337–74 (1986).
[68]M. F. Ashby and S. D. Hallam, ''The Failure of Brittle Solids Containing Small Cracks Under Compressive Stress States,'' *Acta Metall. Mater.,* **34** [3] 497–510 (1986).
[69]B. R. Lawn, N. P. Padture, F. Guiberteau, and H. Cai, ''A Model for Microcrack Initiation and Propagation Beneath Hertzian Contacts in Polycrystalline Ceramics,'' *Acta Metall.,* **42** [5] 1683–93 (1994).
[70]A. C. Fischer-Cripps and B. R. Lawn, ''Indentation Stress–Strain Curves for ''Quasi-Ductile'' Ceramics,'' *Acta Metall.,* **44** [2] 519–27 (1996).
[71]H. Cai, M. A. S. Kalceff, B. M. Hooks, B. R. Lawn, and K. Chyung, ''Cyclic Fatigue of a Mica-Containing Glass-Ceramic at Hertzian Contacts,'' *J. Mater. Res.,* **9** [10] 2654–61 (1994).
[72]N. P. Padture and B. R. Lawn, ''Fatigue in Ceramics with Interconnecting Weak Interfaces: A Study Using Cyclic Hertzian Contacts,'' *Acta Metall.,* **43** [4] 1609–17 (1995).
[73]B. R. Lawn, A. G. Evans, and D. B. Marshall, ''Elastic/Plastic Indentation Damage in Ceramics: The Median/Radial Crack System,'' *J. Am. Ceram. Soc.,* **63** [9–10] 574–81 (1980). □